THE ASTROPHYSICAL JOURNAL, 471:400–426, 1996 November 1

FAR-INFRARED LINE EMISSION FROM COLLAPSING PROTOSTELLAR ENVELOPES

CECILIA CECCARELLI,[1,2,3] DAVID J. HOLLENBACH,[1] AND ALEXANDER G. G. M. TIELENS[1]
Received 1996 January 16; accepted 1996 May 13

ABSTRACT

We present a theoretical model that computes the chemical evolution, thermal balance, and line emission from the collapsing gas of the envelopes that surround protostars. This is the first attempt to calculate self-consistently the line spectrum from the infalling gas with a model that includes dynamics, chemistry, heating and cooling, and radiative transfer. For the dynamics, we have adopted the Shu "inside-out" spherical collapse of an isothermal cloud valid for $r \geq r_c$, where the centrifugal radius $r_c \sim 10^{14}$–10^{15} cm. A time-dependent chemical code follows the chemical composition of the envelope during the collapse.

The main chemical result is that the inner regions ($r \lesssim 10^{15}$ cm) have high H_2O abundances caused by the evaporation of H_2O ice from grains when dust temperatures exceed $\sim$100 K and by gas-phase chemical reactions when gas temperatures exceed $\sim$200 K. The gas is heated mainly by absorption of (dust continuum) near-infrared (NIR) photons by H_2O molecules in the inner regions, by compressional heating in an intermediate zone, and by collisions of gas with warm dust grains in the outer regions ($r \gtrsim 10^{17}$ cm). The gas is cooled by H_2O rotational lines in the inner regions, by the [O I] 63 μm fine-structure line and CO rotational lines in the intermediate region, and by CO rotational lines in the outer zones. The gas temperature roughly tracks the grain temperature for 10^{14} cm $\leq r \leq 10^{17}$ cm, ranging from about 300 K to 10 K.

We present the computed spectrum of a 1 $M_\odot$ protostar accreting at a rate of 10^{-5} $M_\odot$ yr^{-1}. The H_2O lines and the [O I] 63 μm line will be easily detectable by the spectrometers on board the Infrared Space Observatory (ISO). The [O I] 63 μm line and the mid J ($J \sim 7$–15) CO lines can be detected by the Kuiper Airborne Observatory (KAO) or the Stratospheric Observatory For Infrared Astronomy (SOFIA), and certain low-J CO lines can be detected by ground-based telescopes. We present also a large number of other models in which we test the sensitivity of the spectrum to the variations in the three main parameters of our model: the inner radius of spherically symmetric infall (e.g., the centrifugal radius), the amount of H_2O ice evaporated into the gas, and the mass accretion rate. We show how H_2O lines, CO lines, and the [O I] 63 μm line can be used to estimate these three parameters and how resolved line profiles will show the velocity signature of the collapse. Comparison between an infalling and static envelope with similar density, chemical, and dust temperature structure shows that line fluxes alone are not enough to unmistakably distinguish the two cases. Observable H_2O masers may be produced in the innermost collapsing gas at $r \sim 4 \times 10^{14}$ cm.

Subject headings: circumstellar matter — line: formation — masers — stars: formation — stars: pre–main-sequence

1. INTRODUCTION

Stars form by the collapse of molecular cloud cores. For low-mass ($M_* \lesssim 4\ M_\odot$) stars, the luminosity of a protostar is derived mainly from the gravitational energy of the infalling gas. This accretion luminosity is absorbed by the circumstellar dust and reradiated as infrared continuum. Considerable theoretical work has focused on the resulting *continuum* spectrum (see, for example, Adams & Shu 1985, 1986; Wolfire & Cassinelli 1986; Natta 1993; Whitney & Hartmann 1993).

In this paper we present a theoretical model for the infrared and submillimeter *line* spectrum produced by the infalling gas around low-mass protostars. We include chemistry, thermal balance, radiative transfer, and a simple spherical collapse model (Shu 1977) in order to calculate the time-dependent gas temperature profile and line spectrum of the infalling gas. We show how the line fluxes provide a unique diagnostic of the density, temperature, and chemical structure at characteristic distances of 10^{14}–10^{16} cm. Line profiles and line widths diagnose collapse and velocity structure, and, together with the line fluxes, the mass infall rate. The derived mass infall rate can be compared to the accretion luminosity in order to diagnose whether the mass accretion flow inside $r \leq 10^{14}$ cm is steady, or whether it is time dependent, producing low-luminosity intervals interspaced with FU Orionis outbursts as in some current models (Bell & Lin 1994).

The adopted spherical collapse of Shu (1977) assumes that cores begin the collapse to form a low-mass star from an initial isothermal equilibrium state in which the gas density $n \propto r^{-2}$. The collapse begins at the (singular) center and moves outward at the sound speed, the so-called inside-out collapse. The mass accretion rate $\dot{M}$ is constant in time and depends only on the sound speed in the isothermal core; typically $\dot{M} \sim 10^{-5}\ M_\odot$ yr^{-1}. If this mass accretes steadily onto a 1 $M_\odot$ central star, the accretion luminosity L_* is $\sim$60 $L_\odot$. This luminosity heats the dust grains to temperatures $\geq$100 K at a characteristic distance of 10^{15} cm. The molecular hydrogen density of the infalling gas at this distance is $\sim 10^7$ cm^{-3}.

[1] NASA Ames Research Center, Moffett Field, CA, 94035-1000.
[2] CNR-Istituto di Fisica dello Spazio Interplanetario, CP27, 00044 Frascati, Italy.
[3] Present address: Observatoire de Grenoble, BP53-F-38041 Grenoble, France.

Terebey, Shu, & Cassen (1984) included rotation in the collapse calculation. They showed that significant departures of spherical symmetry occur for $r \leq r_c$, where r_c is a "centrifugal radius" determined by the angular momentum of the initial core. Inside r_c, a rotationally supported Keplerian disk is formed and spherical collapse no longer applies. Typically, $r_c \sim 10^{14}$–10^{15} cm, and therefore we assume that the spherical free-fall collapse solution ceases at an inner radius $r_i \sim r_c$. Galli & Shu (1993a, 1993b) have shown that the presence of an ordered magnetic field through the molecular core may alter the spherical infall at distances $r \leq 10^{16}$ cm, due to the interaction of the infalling neutral gas with the trace amounts of charged particles tied to the magnetic field. The bulk of the infall is thereby channeled to a thick "pseudo disk" whose plane is perpendicular to the average field direction. The disk is "pseudo" in the sense that it is not rotationally supported, but simply a flattened configuration. Once channeled to the equatorial plane and incorporated into the "pseudo disk," the infalling material continues to fall radially toward the central star until it hits the Keplerian disk at $r \sim r_c$. The model proposed in this paper does not apply strictly to such an infall, but it may provide a first approximation even in this case.

To date, solid observational evidence for collapse is scant. Observational searches for velocity signatures have been performed at millimeter wavelengths, using the low-excitation transitions of trace molecules such as CO and CS to probe the infall (e.g., Zhou 1992; Zhou et al. 1993; Zhou 1995; Choi et al. 1995). Zhou (1995) and Choi et al. (1995) have arguably made the most convincing observation in the source B335. However, these millimetric transitions tend to be dominated by emission at distances greater than 10^{16} cm from the protostar, where the infall velocity (≤ 1 km s^{-1}) is comparable to turbulent and other macroscopic velocity fields, making the unambiguous detection of infall difficult.

Another approach has been to compare continuum observations with the continuum predicted by theoretical infall models. In the Shu (1977) collapse, the infalling region has a density profile $n \sim r^{-3/2}$. Several authors (Butner et al. 1991; Barsony & Chandler 1993; André, Ward-Thompson, & Barsony 1993) have searched for evidence of such density profiles using far-IR continuum measurements. Although a few cases appear consistent with $n \sim r^{-3/2}$, the uncertainties in grain IR emissivities, for example, make it difficult to definitively prove infall by this method.

This paper is the first attempt at self-consistently calculating the line spectrum from the infalling gas by including dynamics, chemistry, heating and cooling, and radiative transfer. However, several earlier theoretical papers have analyzed some aspects of the problem. Gerola & Glassgold (1978) followed the time-dependent chemistry of the collapse of a massive cloud ($M = 2.5 \times 10^4\ M_\odot$). Tarafdar et al. (1985) followed the time-dependent chemistry of the collapse of an initially constant density diffuse cloud, focusing on the hydrodynamics and the chemical evolution of the gas at $r \gtrsim 10^{16}$ cm. The gas temperature was not calculated but estimated "empirically," and no spectra were calculated. Walker, Narayan, & Boss (1994) linked hydrodynamics and radiative transfer to produce millimeter and submillimeter line profiles from nonspherical, collapsing, rotating protostellar systems.

In § 2 we describe our theoretical model, which includes dynamics, chemistry, detailed radiative transfer, and energy balance (heating and cooling). In § 3 we outline our computational method, and in §§ 4–6 we present the results, which include the radial dependence of the chemical composition, the heating and cooling, and the gas temperature as well as the resultant emitted spectrum. Finally, in § 7 we compare our estimated line fluxes with the available observed data. Section 8 summarizes the main results of the paper.

2. THE MODEL

The computation of the line emission from a collapsing envelope surrounding a protostar involves the simultaneous solution of several problems: the dynamical evolution of the envelope, the chemical evolution of the infalling gas, the radiative transfer in the cooling lines, and the thermal balance of the gas and dust as the central object increases in mass and luminosity. In this work we use a modular approach to the problem, partially separating these four parts and checking a posteriori the self-consistency of the results.

2.1. *The Structure and Dynamics of the Protostellar Envelope*

2.1.1. *Gasdynamics and Core Evolution*

We assume that the initial state of the envelope is described by an isothermal sphere in hydrostatic equilibrium (Shu 1977). The molecular hydrogen number density distribution $n_{H_2}(r)$ is then given by

$$n_{H_2}(r) = \frac{a^2}{2\pi\mu m_H G} r^{-2} = 6.3 \times 10^8 \left(\frac{a}{0.35 \text{ km s}^{-1}}\right)^2 r_{15}^{-2} \text{ cm}^{-3}, \quad (1)$$

where a is the sound speed, m_H is the hydrogen mass, μ is the mean molecular mass in amu units, equal to 2.8, r is the distance from the center, $r_{15} = r/10^{15}$ cm, and G is the gravitational constant.

At $t = 0$, the equilibrium is perturbed and the collapse starts from inside out, propagating with the sound speed (Shu 1977). In the inner collapsing regions, the density is described by the free-fall solution:

$$n_{H_2}(r) = \frac{1}{4\pi\mu m_H}\left(\frac{\dot{M}}{2Gt}\right)^{1/2} r^{-3/2} = 2.2 \times 10^7 \left(\frac{\dot{M}_{-5}}{t_5 r_{15}^3}\right)^{1/2} \text{ cm}^{-3}. \quad (2)$$

The free-fall velocity is given by

$$v(r) = \left(\frac{2G\dot{M}t}{r}\right)^{1/2} = 5.15\left(\frac{\dot{M}_{-5} t_5}{r_{15}}\right)^{1/2} \text{ km s}^{-1}, \quad (3)$$

where $\dot{M}$ is the mass accretion rate, related to the sound speed by

$$\dot{M} = 0.975 \frac{a^3}{G} = 10^{-5}\left(\frac{a}{0.35 \text{ km s}^{-1}}\right)^3 M_\odot \text{ yr}^{-1}. \quad (4)$$

$\dot{M}_{-5}$ is $\dot{M}$ in units of $10^{-5}\ M_\odot$ yr^{-1}, and t_5 is the time t in units of 10^5 yr.

The protostellar envelope therefore includes both the free fall region (eq. [2]) and the outer static region (eq. [1]). The interface of these two regions moves outward in time at roughly the sound speed. We use the complete solution for

the inside-out collapse given by Shu (1977). Moreover, in the standard model we assume that during the collapse the core accretes its mass M_* at a constant rate $\dot{M}$ (Stahler, Shu, & Taam 1980). The gravitational energy of the collapsed mass is released radiatively as material falls onto the core radius R_* (which is a function of M_* and $\dot{M}$: Stahler 1988), so that the luminosity L_* of the central object is

$$L_* = \frac{GM_*\dot{M}}{R_*} = 22\left(\frac{M_*}{M_\odot}\right)\dot{M}_{-5}R_{12}^{-1}\ L_\odot\ , \qquad (5)$$

where $R_{12} = R_*/10^{12}$ cm. We also run a model with a lower value of L_*, corresponding to accumulation of mass in the disk. In addition, the mass accretion rate onto the protostar may be somewhat less than the infall accretion rate if a strong protostellar wind is launched from the disk at $R > R_*$.

2.1.2. *The Dust Model*

As material accretes onto a protostar, most of the resultant luminosity is absorbed by the dust in the envelope. We adopted the Adams & Shu (1985) model for the dust temperature profile of the envelope. In this model, the dust temperature T_d is given by the combination of two terms that account for the optically thick and thin parts of the envelope, respectively:

$$T_d(r)^4 = (\alpha T_a r_{15}^{-5/6})^4 + (\beta T_b r_{15}^{-2/5})^4\ , \qquad (6)$$

where

$$T_a = 16.4(\dot{M}_{-5})^{1/3}\left(\frac{M_*}{M_\odot}\right)^{-1/6}\left(\frac{L_*}{L_\odot}\right)^{1/3}\ \mathrm{K}\ , \qquad (7)$$

$$T_b = 47.0\left(\frac{L_*}{L_\odot}\right)^{1/5}\ \mathrm{K}\ . \qquad (8)$$

The two coefficients α and β have been tabulated by Adams & Shu (1985) for different mass accretion rates and masses of the core, as best fits to the results of their radiative transfer computations. The values for our standard model ($L_* = 65\ L_\odot$, $M_* = 1\ M_\odot$, and $\dot{M}_{-5} = 1$) are $\alpha = 0.623$ and $\beta = 1.45$.

In order to calculate the IR continuum radiation field from the dust and to calculate the dust extinction for the emergent line emission from the gas, it is necessary to specify the wavelength-dependent dust opacity. For $\lambda \leq 20$ μm, we adopted the dust opacity curve by Koornneef (1983) (see also Draine 1988), while for $\lambda > 20$ μm we used the dust opacity from Adams & Shu (1985).

2.2. *Chemistry*

2.2.1. *Time-dependent Chemical Model*

Our standard case adopts for the initial conditions the equilibrium chemical abundances at $t = 0$ at the boundary of the envelope ($r \sim 10^{17}$ cm, $n_{H_2} \sim 10^4$ cm^{-3}), which we assumed valid at all radii (i.e., density). This is equivalent to assuming that the chemical composition remained unchanged during the first phase of the condensation of the matter into a singular sphere or, in other words, that the timescale of the condensation was much shorter than the chemical timescale. The other extreme is that the condensation timescale is much longer than the chemical one (for example, if the contraction is driven by the ambipolar diffusion; Lizano & Shu 1989), so that one should start from a situation of chemical equilibrium at each radius (density) of the initially isothermal envelope. Fortunately, we have found that the results are quite independent of the initial conditions *as long as we start with the same abundances of the initially dominant species* H_2, CO, O, and O_2. In either of the two initial conditions described above, the abundances (relative to hydrogen nuclei) are the following radius-independent values: $x(H_2) = 0.5$ (fully molecular), $x(CO) = 3 \times 10^{-4}$ (all C in CO), $x(O_2) = 8 \times 10^{-5}$ (most remaining O in O_2) and $x(O) = 4 \times 10^{-5}$. The equilibrium abundances of O and O_2 are very insensitive to density. In the initial stages of the collapse, ion-molecule chemistry is sufficiently rapid to drive the *minor* species into equilibrium relative to the major species. However, as the collapse proceeds and the gas and dust reach temperatures larger than about 100 K (the so-called hot core phase), H_2O rapidly becomes a major species, the gas-phase chemistry does not have time to adjust to equilibrium, and time-dependent chemistry is required (Brown et al. 1989; Charnley, Tielens, & Millar 1992).

Hence, we solve the time-dependent equations for the chemical composition, taking into account that the chemical species fall continuously from the outer to the inner regions of the envelope.

2.2.2. *The Chemical Network*

In this work, our first aim is to compute the gas temperature profile and the emission spectrum of the dominant coolants such as O, CO, and H_2O. Thus, the main purpose of the chemical network is to compute the abundance of these three species. Our network, detailed in Appendix A, included a total of 44 species, most being oxygen- and/or carbon-bearing molecules, and 182 gas-phase reactions. We include polycyclic aromatic hydrocarbons (PAHs) and their ions in the chemistry in order to follow the charge balance of the dense gas.

The gas-phase *elemental* abundances per H nuclei are reported in Table 1. Values are those given by Jenkins, Jura, & Loewenstein (1983) for ζ Oph, for which the carbon abundance is their upper limit, equal to the value in the Orion Nebula (Peimbert 1982).

2.2.3. H_2O *Formation*

Since H_2O is a key molecule in the cooling of the gas, we will consider its formation processes in some detail. At low temperatures H_2O is formed mainly through standard ion molecule chemistry by the dissociative recombination of the H_3O^+ ion, whose formation can be traced to the cosmic-ray ionization of H_2.

At dust temperatures above about 100 K, icy grain mantles evaporate, injecting a large amount of water into the gas phase. IR observations of objects embedded in or

TABLE 1

ADOPTED GAS-PHASE ELEMENTAL ABUNDANCES (WITH RESPECT TO H NUCLEI)

Element	Abundance
He	0.1
O	5.0E−4
C	3.0E−4
Si	8.0E−7
S	8.0E−6
Mg	1.3E−6
Fe	2.5E−7

located behind molecular clouds show that typically about 10% of the elemental oxygen is in the form of H_2O ice (Tielens 1993). Hence, in our standard model we assume that 10% of the elemental oxygen is injected into the gas phase as H_2O when the dust temperature reaches 100 K, the sublimation temperature of H_2O ice at the low pressures of the envelopes.

Finally, when the gas temperature exceeds about 200 K, reactions with sizable activation barriers start to be efficient, and H_2O formation is dominated by the reaction sequence: $O + H_2 \rightarrow OH + H$; $H_2 + OH \rightarrow H_2O + H$.

2.3. *Radiative Transfer and Level Population Calculation*

The gas is cooled primarily by the [O I] fine-structure lines and the CO and H_2O rotational lines. In order to calculate the gas cooling, we solve the equations of statistical equilibrium for the level populations:

$$n_u \sum_{l=1}^{N_{\rm lev}} (A_{ul} + B_{ul} J_{ul} + C_{ul} + R_{ul}) = \sum_{l=1}^{N_{\rm lev}} n_l (A_{lu} + B_{lu} J_{lu} + C_{lu} + R_{lu}) , \quad (9)$$

$$\sum_{l=1}^{N_{\rm lev}} n_l = n_x , \quad (10)$$

where A_{ul} is the spontaneous transition rate ($A_{ul} = 0$ when $u \leq l$), B_{ul} and B_{lu} are the stimulated emission and absorption coefficients, J_{ul} is the mean intensity of the radiation field at frequency ν_{ul}, C_{ul} is the collisional rate, and R_{ul} is an extra term associated with the NIR photons pumping rate from level u to level l, that we will discuss in detail below. These equations form a highly nonlinear system because the radiation field J_{ul} has contributions both from dust and from the line emission in the gas.

2.3.1. *Radiative Transfer in Presence of Warm Dust*

The treatment of the radiative transfer simplifies greatly in the escape probability formalism (Takahashi, Hollenbach, & Silk 1983):

$$n_u \sum_l (A_{ul} \epsilon_{ul} + B_{ul} J'_{ul} + C_{ul} + R_{ul}) = \sum_l n_l (A_{lu} \epsilon_{lu} + B_{lu} J'_{lu} + C_{lu} + R_{lu}) , \quad (11)$$

where

$$J'_{lu} = J'_{ul} = (\epsilon_{ul} - \eta_{ul}) B(T_d) , \quad (12)$$

is the photon background at the frequency of the u to l transition and is due only to the dust, $B(T_d)$ is the blackbody function at the dust temperature T_d,

$$\epsilon_{ul} = \frac{k_d}{k_L + k_d} + \frac{k_L}{(k_L + k_d)^2} k_\Omega , \quad (13)$$

is the escape probability from line absorption, and

$$\eta_{ul} = \frac{1}{k_L + k_d} k_\Omega , \quad (14)$$

is the escape probability from dust absorption. Here k_L and k_d are the line and dust absorption coefficients, respectively:

$$k_L = \frac{hc}{8\pi \Delta v_{\rm th}} (n_l B_{lu} - n_u B_{ul}) , \quad (15)$$

$$k_d = K_d 2 n_{\rm H_2} , \quad (16)$$

where $\Delta v_{\rm th}$ is the thermal velocity width and K_d is the dust cross section per hydrogen nuclei. Finally, k_Ω is the integral over the solid angle $d\Omega$, given by the following expression:

$$k_\Omega = \int_0^1 d\mu \frac{1 - \exp\left[-(k_L + k_d)\Delta L_{\rm th}\right]}{\Delta L_{\rm th}} . \quad (17)$$

$\Delta L_{\rm th}$ is the size of the line-trapping region, which in the case of accelerated inflow is equal to

$$\Delta L_{\rm th} = 2\Delta v_{\rm th} \left(\frac{v}{r} \left| 1 - \frac{3}{2} \mu^2 \right| \right)^{-1} , \quad (18)$$

in the direction that forms the angle $arccos(\mu)$ with the radial outward direction (Castor 1970). To take into account the finite dimension of the envelope, the actual value of $\Delta L_{\rm th}$ is the minimum between the value given by equation (18) and $\frac{1}{2} r[1 - (r/R_{\rm env})^{1/2}]$. In the static region, the line-trapping length has been approximated by its density-weighted minimum value $\Delta L_{\rm th} = r(1 - r/R_{\rm env})$, where $R_{\rm env}$ is the radius of the envelope.

The escape probability formalism is not strictly applicable to the case of an accelerating infall velocity field because the hypothesis of local radiation trapping fails: each point of the envelope is radiatively coupled with a surface, and the problem should be solved iteratively to find the self-consistent solution of the coupled regions (Grachev & Grinin 1975; Marti & Noerdlinger 1977; Rybicki & Hummer 1978). On the other hand, the exact solution of the radiative transfer in this case would be prohibitive. Our first goal is the computation of the gas temperature profile and, for this purpose, the approximation of neglecting the radiative coupling between different regions of the envelope does not affect the results significantly, since in practice the hot coupled region does not subtend a large solid angle to the cold coupled region (see also Rybicki & Hummer 1978 for a discussion of the error associated with this approximation).

2.3.2. *NIR Photon Pumping*

At each radius r, CO and H_2O molecules can be excited both by the IR continuum due to the warm dust at the same radius r and by the hot dust closer to the center at $r_{\rm NIR}$ (see Appendix B), whose NIR photons pump vibrationally and redistribute the molecules rotationally. The lifetime in the vibrationally excited states is so short that the molecules decay essentially instantaneously to rotational levels of $v = 0$. The net result of the NIR pumps is a redistribution of the $v = 0$ rotational levels, which we characterize by rotational excitation and de-excitation rates R_{lu} and R_{ul} into and out of level u (see eqs. [9] and [11]).

The importance of this pumping depends on the inner dust temperature $T_{\rm NIR}$, on the dilution factor W_d that accounts for the solid angle filled by the hot surface, and on the extinction $\tau_{\rm NIR}$ between r and $r_{\rm NIR}$. In our model we take into account numerically the contribution from regions at distances less than the dust evaporation radius (where the dust temperature is higher than 1600 K) for which $\tau_{\rm NIR}$ is less than or equal to 5. Note that for the calculation of the NIR pumping, we include the emission by very warm dust, which lies inside r_i. Appendix B provides details of the pumping calculation.

2.3.3. *Atomic and Molecular Data*

We consider the [O I] fine-structure lines and the CO and

H_2O pure rotational lines. The [O I] data are taken from Launay & Roueff (1977).

For CO, we consider the first 50 rotational levels of the ground and first vibrational state. For temperatures greater than about 25 K, we follow Hollenbach & McKee (1979) and McKee et al. (1982) for the analytical formulation of the CO collision de-excitation coefficients. For lower temperatures, we use the collision de-excitation coefficients given by Flower & Launay (1985) for the first 11 levels.

For H_2O, we consider the first 45 levels of the ground and of the $v_2 = 1595.0$ cm^{-1} vibrational state of ortho and para water. We assumed a ratio of 3:1 between ortho and para water. The spontaneous emission coefficients and the level energies were taken from the HITRAN database (Rothman et al. 1987), version of 1992 February. The collisional coefficients for the pure rotational transitions are from Green, Maluendes, & McLean (1993).

2.4. *Energy Balance*

Various processes contribute to the heating and cooling of the gas: (i) compression of the collapsing gas, (ii) gas-grain collisions that transfer the energy from the dust to the gas (if the dust is warmer) or vice versa, and (iii) absorption of dust continuum photons, followed by collisional de-excitation. Cooling is dominated by fine-structure line emission of [O I] and rotational line emission by CO and H_2O.

2.4.1. *Cooling and Heating by Line Emission and Absorption*

The net cooling rate Λ for a given species is given by

$$\Lambda = \sum_{u,l} h\nu_{ul}(n_l C_{lu} - n_u C_{ul}) . \tag{19}$$

Using equation (9) for the statistical equilibrium of the level population, equation (19) can be rewritten as

$$\Lambda = \sum_{u,l} h\nu_{ul} A_{ul} \epsilon_{ul} n_u \left(1 - \frac{J'_{ul}}{S_{ul}}\right) + \sum_{u,l} h\nu_{ul}(n_u R_{ul} - n_l R_{lu}) , \tag{20}$$

where S_{ul} is the source function. The first sum represents the line emission, while the second sum represents the (negative) cooling due to the energy input from the NIR photon absorption. To clarify this equation, we define Λ_0 as the cooling rate when the NIR radiation field is zero. Then the following relation holds:

$$\Lambda = \Lambda_0 - \sum_{u,l} h\nu_{ul}(n_l R_{lu} - n_u R_{ul}) + \sum_{u,l} h\nu_{ul} A_{ul} \epsilon_{ul} \Delta n_u \left(1 - \frac{J'_{ul}}{S_{ul}}\right) , \tag{21}$$

where Δn_u is the variation of the level population caused by the NIR photon absorption. Equation (21) can be interpreted easily: the efficiency of gas cooling is reduced by the presence of the hot inner dust, and the second and third terms together represent the heating (negative cooling) resulting from the NIR photon absorption. The second term describes the rotational energy in $v = 0$ excited by the NIR radiation field, and the third term corrects this "heating" term for the energy emitted by radiative decay; that is, only those pumping events that are followed by collisional de-excitation from level u to l lead to heating of the gas. The remainder is merely redistributed in frequency from the NIR to the frequency of the $u \rightarrow l$ transition. If this heating term is greater than the cooling rate, the molecule acts as a heat source, coupling the gas to the high-temperature (NIR) radiation field produced by the hotter material near the star.

In general, however, this effect does not lead to a net heating by CO or H_2O but results in a decrease of the cooling efficiency of the molecule. The heating rate from this NIR photon pumping can thus be expressed as

$$\Gamma_{\rm NIR} = \sum_{u,l} h\nu_{ul}(n_l R_{lu} - n_u R_{ul}) - \sum_{u,l} h\nu_{ul} A_{ul} \epsilon_{ul} \Delta n_u \left(1 - \frac{J'_{ul}}{S_{ul}}\right) . \tag{22}$$

In the thermal balance, we will consider Λ_0 as the cooling term and $\Gamma_{\rm NIR}$ as a heating term.

Appendix B shows how the NIR heating can be solved analytically with some simplifying assumptions for the case of the CO molecule in rotational LTE. In the limit of $T_{\rm NIR} \gg T_{\rm CO}$, the heating becomes

$$\Gamma_{\rm CO} \simeq 8 n_{\rm CO} A_v W_d e^{-\tau_{\rm NIR}} e^{-E_v/kT_{\rm NIR}} E_0 , \tag{23}$$

where $A_v \sim 18.9$ s^{-1} is the spontaneous decay rate from $v = 1$ to $v = 0$ (Chackerian & Tipping 1983), $E_v/k \sim 3126$ K and $E_0/k = 2.7$ K, and W_d is the dilution factor given in Appendix B in equation (30).

The term that describes the line emission (the first term in eq. [20]) can itself become a negative term if $J' \geq S$ (see Takahashi et al. 1983), e.g.,in the presence of a strong FIR continuum. The rotational transitions in this case absorb FIR photons from the dust, and subsequent collisional de-excitation heats the gas. This case can operate only when the local dust is warmer than the gas.

Finally, the flux in a given line from a source at distance d is given by

$$F_{ul} = \frac{1}{4\pi d^2} \int_{r_i}^{\infty} h\nu_{ul} A_{ul} \epsilon_{ul} n_u \left(1 - \frac{J'_{ul}}{S_{ul}}\right) 4\pi r^2 \, dr . \tag{24}$$

2.4.2. *Heating by Gas Compression and Dust-Gas Collisions*

Because we anticipate that the gas temperature gradient is coupled with the shallow grain temperature gradient, most of the compressional heating will be radiated away. In this simplifying limit, we can add a "compressional heating term" to the balance of gas heating and cooling. This heating term is given by

$$\Gamma_{\rm comp} = \frac{5}{2} kT_{\rm gas} v \left| \frac{dn_{\rm H_2}}{dr} \right| , \tag{25}$$

where $T_{\rm gas}$ is the gas temperature and v is the velocity of the gas in that point. Substituting the density gradient power law that holds in the collapsing region, equation (25) becomes

$$\Gamma_{\rm comp} = \frac{15}{4} kT_{\rm gas} \frac{v}{r} n_{\rm H_2} , \tag{26}$$

Gas-grain collisions tend to minimize the dust and gas temperature differences, being a source of heating when the dust temperature is higher than the gas temperature and vice versa. Following Hollenbach & McKee (1979), the energy exchange rate between the dust and the gas is

$$\Gamma_{dg} = n_{\rm H_2} n_d \sigma_d \left(\frac{8kT_{\rm gas}}{\pi m_{\rm H_2}}\right)^{1/2} 2k(T_d - T_{\rm gas})\alpha \tag{27}$$

where n_d and σ_d are the dust density and grain cross section, respectively, and $\alpha(\sim 0.2$–$1.0)$ is the accommodation coefficient (Burke & Hollenbach 1983; Takahashi et al. 1983).

3. COMPUTATIONAL METHOD AND MODEL PARAMETERS

3.1. *Computational Method*

Figure 1 shows a schematic diagram of the elements of the computation and their interrelation. The computation of the line spectrum requires, at each instant of time, knowledge of the radial dependences of the gas and dust temperature, the infall velocity, the dust radiation field, and the abundances of the chemical species. Obviously, the chemical abundances depend on the gas temperature because of the temperature sensitivity of the chemical rates, and at the same time the gas temperature depends on the abundances of the dominant coolants. Note that the chemical composition depends also on the dust temperature, since H_2O evaporates from the grains into the gas when the dust temperature reaches 100 K. The heating rate depends mainly on the dust temperature, which controls gas-grain collisional heating and NIR pump heating, and the free-fall velocity, which controls the compressional heating. The NIR pump heating is affected also by the chemical composition, which determines the abundances of NIR absorbers.

The first great simplification to the problem is the separation of the dynamical and thermal evolution of the system. Although in principle they are tied together, we adopted the "simple" dynamical solution of spherical isothermal collapse and separated the two problems. In addition, the dust opacity and temperature are taken from the solution of existing models in literature (Adams & Shu 1985) and are computed separately.

With this simplification, the behavior of the infalling gas reduces to the problem of solving the time-dependent chemistry and the thermal balance at each point of the envelope as a function of time. To minimize computational complexity, we followed an iterative procedure. First we solve the time-dependent chemistry to obtain chemical abundances assuming the gas temperature to be equal to the dust temperature. Then, using the derived chemical abundances, we compute the cooling and heating rates from § 2.4 and calculate the gas temperature from the thermal balance. Finally, we recompute the chemical abundances with the new gas temperature profile and check that the abundances and energy line spectra do not change appreciably. One such iteration generally suffices. After running a number of models, we found a posteriori that the abundances of the dominant coolants O, CO, and H_2O can be estimated analytically at each point (see § 4.2 below). Therefore, utilizing the analytic estimates, even the single iteration is not necessary, and one can "separate" the chemical and thermal evolution of the system as well.

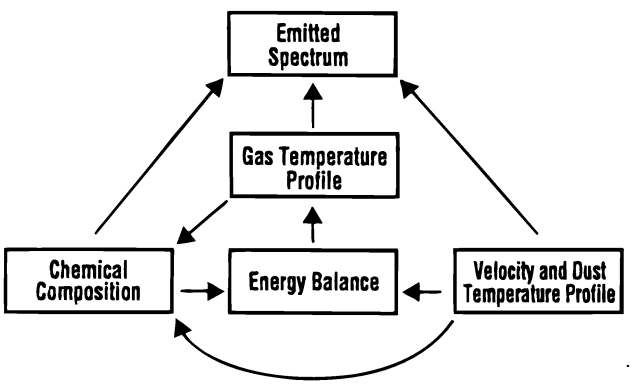

FIG. 1.—Diagram of the processes involved in the computation of the line emission from collapsing envelopes.

The time-dependent equations for the chemical composition of the envelope are solved using the Gear (1971) algorithm for the solution of "stiff" coupled differential equations. We have checked the chemical code by running various cases until steady state is achieved and comparing the results against previously calculated steady state results.

3.2. *The Adopted Parameters for the Models*

3.2.1. *The Standard Case*

Our model depends primarily on three key parameters: the mass accretion rate, the inner radius $r_i \sim r_c$, and the amount of water evaporated from the grain mantles when the dust is warm. We considered some reasonable values for our standard model, but we also ran several cases in order to study the dependence of our results on these parameters.

Our standard model studies the collapse of 1 $M_\odot$ protostar accreting material from its envelope at a rate of 10^{-5} $M_\odot$ yr^{-1}; this value corresponds to a sound speed of 0.35 km s^{-1}. The luminosity of the source increases almost linearly with time (eq. [5]); at the end of the collapse ($M_* = 1\ M_\odot$), it reaches a value of 65 $L_\odot$. We take $r_i = 3 \times 10^{14}$ cm ($\sim$20 AU), since the spherical approximation probably breaks down closer to the center, at which the presence of a centrifugal disk plays a major role in the collapse (Terebey et al. 1984). In the standard case, we evaporate water ice when the grain temperature reaches 100 K, injecting into the gas phase an abundance 6×10^{-5} of H_2O, i.e., 10% of the cosmic elemental oxygen. The gas-phase elements are otherwise given as in Table 1, and the initial abundances of species are given in Table 2. We follow the time evolution of the infalling envelope and present the results of the computation at different times.

3.2.2. *The Other Cases*

We have run 17 other cases with the aim of probing the sensitivity of the computed line fluxes to the parameters of the model. To make the comparison and the interpretation as simple as possible, in the spirit of an "observational approach," we considered sources with two different (late-time) luminosities: a moderate-luminosity source, 20 $L_\odot$, and a relatively brighter source of 65 $L_\odot$. Observationally, the luminosity of the source is determined readily from the measured IR continuum. For each case, we fixed the luminosity at one of these two values and varied the three key parameters: the inner radius r_i, the amount of water ice on grains, and the mass accretion rate. Table 3 summarizes the adopted parameters for all the cases studied.

The value of r_i, i.e., the radius at which angular momentum converts spherical accretion into a centrifugal disk, depends on the initial angular momentum of the core (Terebey et al. 1984). We varied r_i from 3×10^{14} cm to 1×10^{14} cm and 3×10^{13} cm. Our goal is to determine which observable lines are insensitive to r_i and can therefore constrain the other two parameters of the model, and conversely, which lines depend strongly on it and can provide probes of the warm component in the inner region ($r \leq 3 \times 10^{14}$ cm).

We also varied the fraction of evaporated ice in the warm regions in which the dust temperature is greater than 100 K

TABLE 2

INITIAL FRACTIONAL ABUNDANCES (WITH RESPECT TO H NUCLEI)

Species	Abundance
H	4.1(−5)
He	1.0(−1)
C	1.7(−9)
O	3.9(−5)
Si	4.2(−7)
S	8.0(−6)
Mg	1.3(−6)
Fe	2.5(−7)
H_2	0.5
CH	8.5(−13)
OH	1.2(−8)
SiH	1.4(−11)
CO	3.0(−4)
O_2	8.0(−5)
SiO	3.8(−7)
CH_2	5.0(−11)
H_2O	1.9(−7)
e^-	6.3(−10)
H^+	1.1(−10)
He^+	1.0(−11)
C^+	4.2(−11)
O^+	2.6(−15)
Si^+	4.5(−11)
S^+	2.5(−10)
Mg^+	9.0(−11)
Fe^+	7.0(−11)
H_2^+	6.0(−14)
CH^+	3.1(−17)
OH^+	1.0(−14)
CO^+	2.5(−15)
SiO^+	1.1(−17)
H_3^+	1.1(−10)
CH_{2+}	9.0(−17)
H_2O^+	1.9(−14)
SiH_2^+	7.5(−13)
HCO^+	7.8(−9)
$HOSi^+$	2.5(−12)
CH_3^+	1.4(−12)
H_3O^+	8.0(−10)
H^-	4.9(−18)
PAH	9.1(−8)
PAH^-	8.8(−9)
PAH^+	2.5(−12)
$PAHH^+$	3.5(−11)

NOTE.—$a(b) = a \times 10^b$.

TABLE 3

PARAMETER VALUES FOR EACH MODEL

Model	$L(L_\odot)$	$M(M_\odot)$	r_i(cm)	H_2O/Oxygen	$M(M_\odot\ yr^{-1})$
1	65	1.00	3E14	0.10	1E−5
2	65	1.00	1E14	0.10	1E−5
3	65	1.00	3E13	0.10	1E−5
4	65	1.29	3E14	0.10	5E−6
5	65	3.24	3E14	0.10	2E−6
6	65	1.00	3E14	0.00	1E−5
7	65	1.00	3E14	0.01	1E−5
8	65	1.00	3E14	0.30	1E−5
9	20	0.16	3E14	0.10	1E−5
10	20	0.16	1E14	0.10	1E−5
11	20	0.16	3E13	0.10	1E−5
12	20	0.20	3E14	0.10	5E−6
13	20	1.00	3E14	0.10	2E−6
14	20	0.16	3E14	0.00	1E−5
15	20	0.16	3E14	0.01	1E−5
16	20	0.16	3E14	0.30	1E−5
17	20	1.00	3E14	0.10	1E−5
18[a]	65	1.00	3E14	0.10	0

[a] Static envelope.

from 30% of the cosmic oxygen abundance to no evaporation at all. This is a poorly known parameter, and our goal is to identify observable lines that will measure the evaporated ice content.

The last key parameter is the mass accretion rate: we ran cases of $2 \times 10^{-6}\ M_\odot\ yr^{-1}$, $5 \times 10^{-6}\ M_\odot\ yr^{-1}$, and $1 \times 10^{-5}\ M_\odot\ yr^{-1}$. The first value of the accretion rate may approximate the collapse better in cold clouds such as the Taurus Auriga complex. We notice that to keep the source luminosity fixed, the central mass of the object is different in each case, as the luminosity depends on both the mass accretion rate and the central mass.

We also ran a case of "interrupted" mass accretion. This model has the same mass accretion rate outside r_i as the standard model, but we assume that this mass accumulates or is lost in a wind at a relatively large distance ($r \gg R_*$) from the star, so that the accretion luminosity is lower than the standard case. We adopted $L_* = 20\ L_\odot$, i.e., a luminosity more than 3 times lower than $\dot{M}$, M_*, and R_* would predict via equation (5). Steady accretion has been challenged by Lin & Pringle (1990) and Bell & Lin (1994), who argue that mass may build up at $r \sim 10^{12}$–10^{13} cm and then be released onto the star in short ($\sim$100 yr) bursts that give rise to the FU Orionis phenomena. In this case, much of the life of the protostar is spent with high outer ($r \gtrsim 10^{13}$ cm) accretion rates but low luminosity. This may explain why so few embedded sources are observed with luminosities greater than few solar luminosities.

Finally, we ran the case of a static envelope surrounding a 65 $L_\odot$ source. In this case the density profile, chemical composition, and dust temperature profile are chosen to be very similar to the infalling envelope of our standard case. The goal is to find differences in the two line spectra (static vs. infalling) that can be attributed to the velocity field of the envelope.

4. THE CHEMICAL STRUCTURE OF THE ENVELOPE

4.1. *The Standard Case*

In Figure 2 we show the radial profile of the dust temperature profile (§ 2.1.2) (recall that the gas temperature is initially assumed to be equal to the dust temperature in the calculation of the chemical abundances), the H_2 density, and the fractional abundances of some important molecules at different times as a function of r. We discuss below the chemistry of these molecules.

4.1.1. *Charge Carriers and Degree of Ionization*

PAH^- is the dominant negative charge carrier across the entire envelope; electrons are a factor 3–300 lower in abundance (Fig. 2*b*). PAH^- is formed by electron attachment to PAHs and destroyed by collisions with $PAHH^+$, which is the dominant ion in the inner regions, and with H_3O^+ and HCO^+ in the outer regions, in which they dominate the positive ion balance.

$PAHH^+$ results from the proton exchange of HCO^+ with PAH. HCO^+ and H_3O^+ are formed through a chain of reactions initiated by the cosmic-ray ionization of molecular hydrogen and followed by ion-molecule reactions that tend to protonate various species (see Appendix A).

The degree of ionization (i.e., the PAH^- and the dominant positive ion abundance) scales, as expected, with $n_{H_2}^{-1/2}$, since cosmic-ray ionization per unit volume scales with n_{H_2} (charge creation) while charge destruction scales with $n_{H_2}^2 x_{PAH^-}^2$ (mutual neutralization by PAH^+ collisions

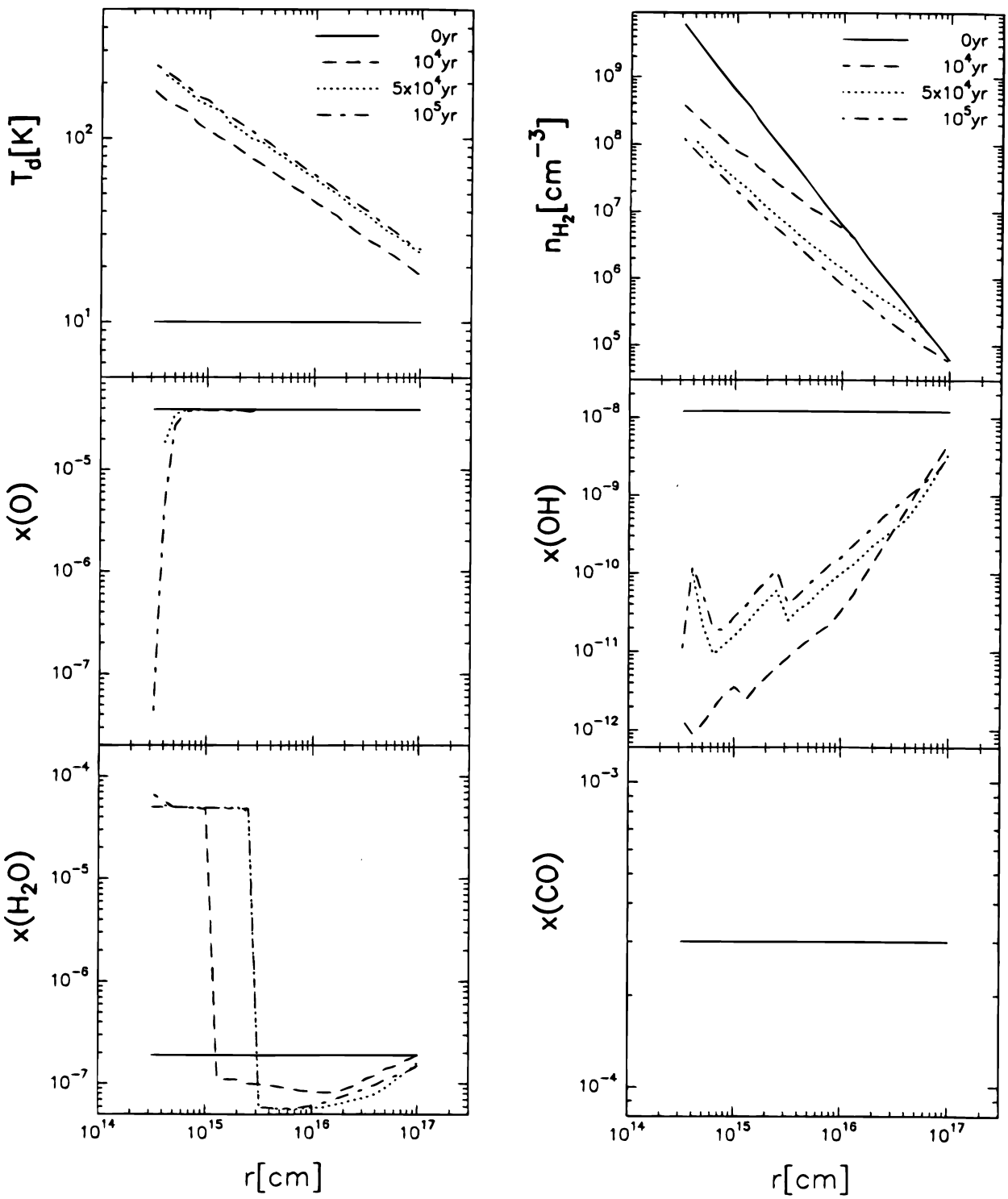

FIG. 2a

FIG. 2.—The dust temperature, H_2 density profile, and fractional abundances of species with respect to H nuclei for a protostar accreting at $10^{-5}\ M_\odot\ \mathrm{yr}^{-1}$ (after Shu 1977 and Adams & Shu 1985) at the start of the collapse (*solid line*) and at 10^4 yr (*dashed line*), 5×10^4 yr (*dotted line*), and 10^5 yr (*dash-dotted line*) from the start of the collapse.

with ions). However, the electron abundance scales as

$$x_e = 4.4 \times 10^{-5} \left(\frac{x_{\mathrm{PAH}}}{10^{-7}} \right)^{-1} n_{\mathrm{H_2}}^{-1} . \qquad (28)$$

In Figure 2*b*, the $n_{\mathrm{H_2}}^{-1}$ dependence of x_e can be seen easily. Note that the abundances of HCO^+ and H_3O^+ can exceed x_e because the negative charge is carried by PAH^-. The jump in H_3O^+ is caused by the evaporation of ice from the grains, which injects H_2O into the gas and leads to H_3O^+ production ($H_2O + H_3^+ \rightarrow H_3O^+ + H_2$). The drop in HCO^+ is caused by proton transfer with H_2O, which becomes suddenly more abundant when ice evaporates.

4.1.2. *Molecular Abundances*

At the beginning of the evolution, almost all the oxygen is in CO, O_2, and O, with percentages of 60%, 32%, and 8%, respectively. The CO and O_2 abundances are quite constant in the envelope and do not vary appreciably with time.

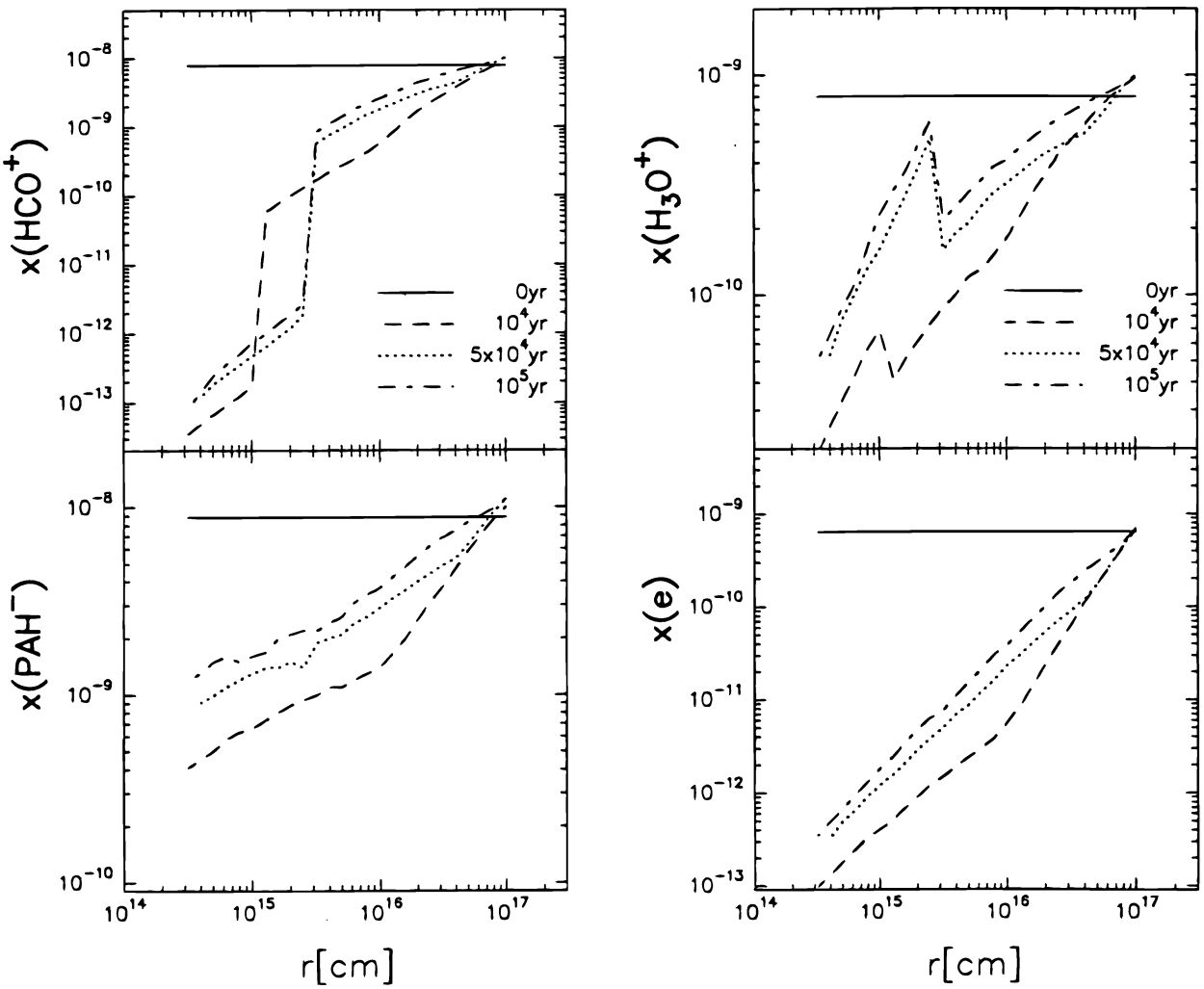

FIG. 2*b*

In the initial stages of the collapse, standard ion-molecule chemistry regulates the abundance of OH and H_2O (see § 2.2.4). OH and H_2O are destroyed by reactions with C^+ forming CO^+ and HCO^+, which lead to CO. OH is also destroyed by reaction with O to form O_2.

At later stages in the innermost regions, the oxygen budget changes significantly when H_2O ice evaporates at $T_d \geq 100$ K. At somewhat higher temperatures ($T_{gas} \geq 200$ K), the reaction $O + H_2$ initiates the conversion of atomic oxygen into H_2O. Figure 2 shows a rapid drop in the O abundance in the inner regions signifying this conversion. The large amount of injected water is slowly redistributed into OH through reaction with H_3^+ followed by dissociative electron recombination of H_3O^+ with PAH^- on a timescale $\geq 10^5$ yr [see rise in x(OH) with time in Fig. 2]. Initially this OH is converted into O_2 via the reaction of OH with O; at later times ($\geq 5 \times 10^4$ yr), the gas temperature is so high that the $OH + H_2$ reaction, which reforms H_2O, dominates over OH + O. The destruction of O_2 by He^+ and C^+ occurs on too slow a timescale ($\sim 3 \times 10^7$ yr), compared to a collapse timescale of 10^5 yr, to convert an appreciable amount of O_2 into O and eventually H_2O in the dense, warm gas. In summary, the oxygen-bearing molecules serve as a chemical memory of the important processes taking place during collapse. H_2O largely reflects the evaporation of icy grain mantles at $r \sim 10^{15}$ cm and warm gas-phase chemistry in the innermost regions $r \lesssim 3 \times 10^{14}$ cm.

4.2. *The Other Cases*

The results of our model suggests a simple analytic paradigm for the abundances of the important coolants O, CO, and H_2O. Essentially all gas-phase carbon is in CO (an abundance of 3×10^{-4} in our models). The atomic oxygen abundance is constant (4×10^{-5} in our models) for gas temperatures less than 200 K and extremely small at higher temperatures. The H_2O abundance is low and constant (1.5×10^{-7} in our models) for $T_d < 100$ K and $T_{gas} < 200$ K. When $T_d > 100$ K, an amount of gas-phase H_2O equal to the H_2O ice content is added to the H_2O abundance. When $T_{gas} > 200$ K, the abundance of H_2O increases by about 1.5×10^{-5}, due to the partial conversion of O to H_2O.

5. THE THERMAL STRUCTURE OF THE ENVELOPE

5.1. *The Standard Case*

In Figure 3 we plot the gas and dust temperature profiles. The contributions to the cooling of the gas across the envelope include [O I] fine-structure line emission, CO and H_2O cooling by rotational line emission in absence of the NIR photon absorption, i.e., the Λ_0 term of equation (21), and cooling by collisions of the gas with the dust, when the gas is warmer than the dust. The contributions to the

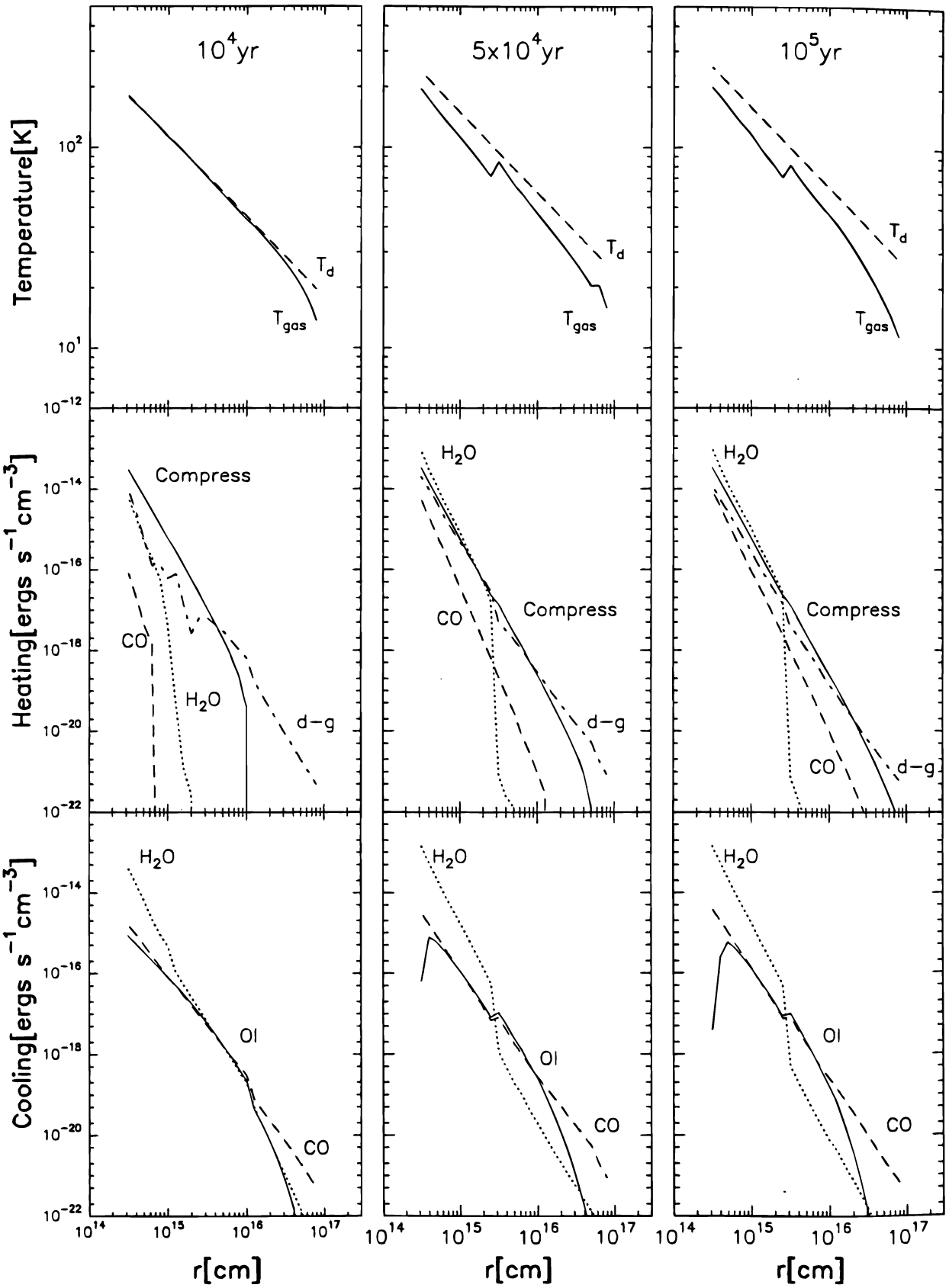

FIG. 3.—Gas and dust temperature profiles and the heating and cooling rates of a protostar accreting at $10^{-5}\ M_{\odot}\ \mathrm{yr}^{-1}$ at 10^4 yr (*left*), 5×10^4 yr (*middle*), and 10^5 yr (*right*) from the start of the collapse. Contributions to the gas heating feature the gas compression from the collapse (*solid line*), gas-grain collisions (*dash-dotted line*), H_2O (*dotted line*), and CO (*dashed line*) NIR photopumping heating, as described in the text. Gas cooling is dominated by the H_2O (*dotted line*) and CO (*dashed line*) rotational line emission and the [O I] 63 μm fine-structure line emission (*solid line*).

heating include compressional heating, heating by the gas-grain collisions, when the gas is colder than the dust, and NIR photopump heating via CO and H_2O computed according to equation (22). Of special note is how closely T_{gas} tracks T_d. We discuss separately the inner, intermediate, and outer regions.

5.1.1. *Inner Region*

The inner region is defined as the region in which the dust temperature exceeds 100 K, so that a large amount of water vapor is released by icy grain mantles. The inner region is roughly at

$$r \lesssim 3 \times 10^{15} (L_*/65\ L_\odot)^{1/2}\ \text{cm}$$
$$= 2 \times 10^{15} (t_5)^{1/2} (\dot{M}_{-5}) R_{12}^{1/2}\ \text{cm} .$$

The gas and dust temperatures differ about 35%, i.e., they are relatively well coupled; the coupling is better at smaller radii. At early times, gas cooling in this region is dominated by H_2O rotational line emission, while heating is mainly due to compression of infalling gas. At later times ($t \geq 5 \times 10^4$ yr), the thermal balance in this region is determined by the thermostating action of water vapor in the presence of an NIR field. In a sense, H_2O provides most of the heating and cooling of the gas at later times. In other words, the gas temperature adjusts until the H_2O cooling exceeds slightly the NIR "heating," so that the net cooling can offset the additional compressional heating.

CO molecules are a net source of heating to the gas because NIR pump heating by dust continuum photons overcomes cooling by rotational transitions. The drop in [O I] cooling in the innermost region is caused by the conversion of atomic oxygen into molecular oxygen and water.

5.1.2. *Intermediate Region*

The intermediate region is defined by 3×10^{15} cm $\lesssim r \lesssim 10^{16}$ cm, where $T_{gas} \sim T_d \sim 50$–100 K. In this zone, most of the H_2O is frozen out on grains and cooling is dominated by [O I] 63 μm and CO rotational lines. CO and H_2O NIR photopumping in this region is relatively negligible, and heating is dominated by compression of infalling gas. The inner/intermediate transition is marked by a jump of the gas temperature as both [O I] and CO are less efficient in cooling the gas than H_2O. Gas and dust temperatures differ by about 25%.

5.1.3. *Outer Region*

At distances greater than about 10^{16} cm at which the gas temperature drops below 50 K, CO cooling dominates. Heating is dominated by gas-grain collisions, although compressional heating still contributes to gas heating in the collapsing region.

5.2. *The Other Cases*

We discuss separately how the heating, cooling, and the gas temperature profile depend on inner radius, H_2O ice abundance, and mass infall rate.

5.2.1. *Inner Radius*

The temperature profiles with small inner radius $r_i = 3 \times 10^{13}$ cm for both 20 $L_\odot$ ($M_* = 0.16\ M_\odot$, model 11) and 65 $L_\odot$ ($M_* = 1\ M_\odot$, model 3) are compared in Figure 4. In the inner regions the gas is always colder than the dust, with the percentage difference increasing slightly going outward.

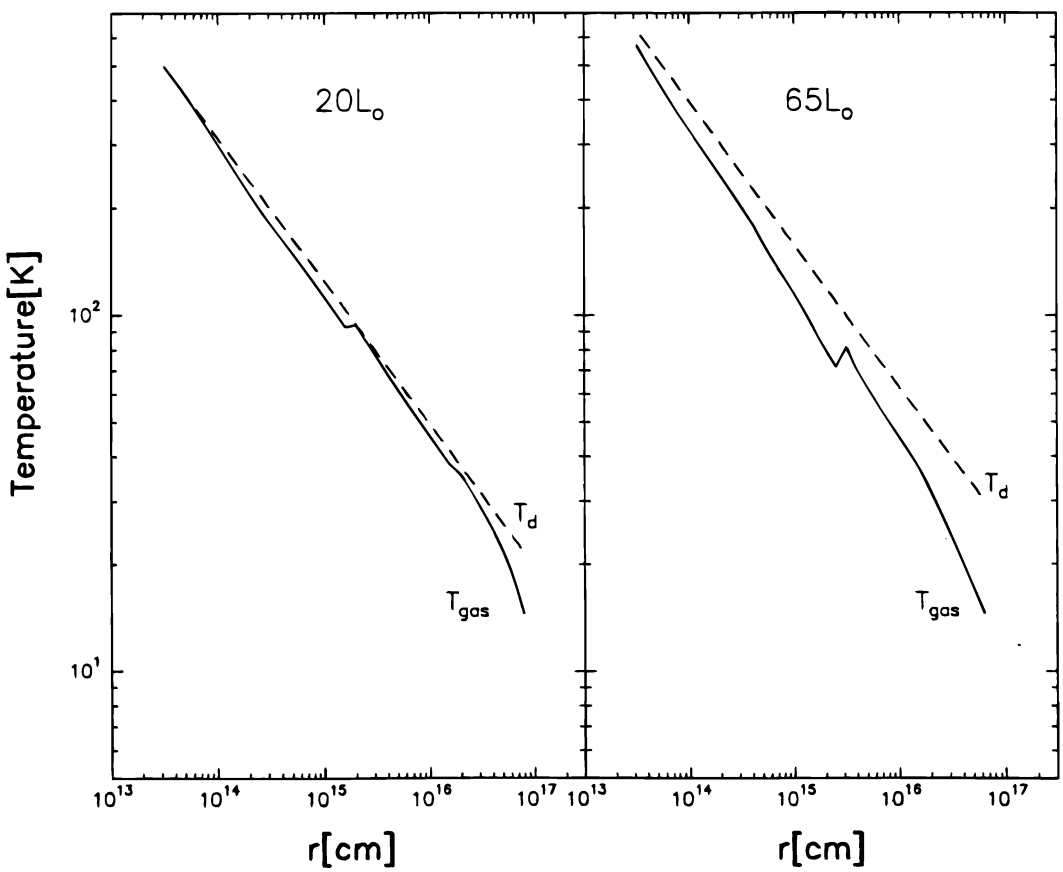

FIG. 4.—Gas and dust temperature profiles starting at $r = 3 \times 10^{13}$ cm of 0.16 $M_\odot$ protostar (20 $L_\odot$, *left*) and 1 $M_\odot$ protostar (65 $L_\odot$, *right*) accreting at $10^{-5}\ M_\odot\ \text{yr}^{-1}$.

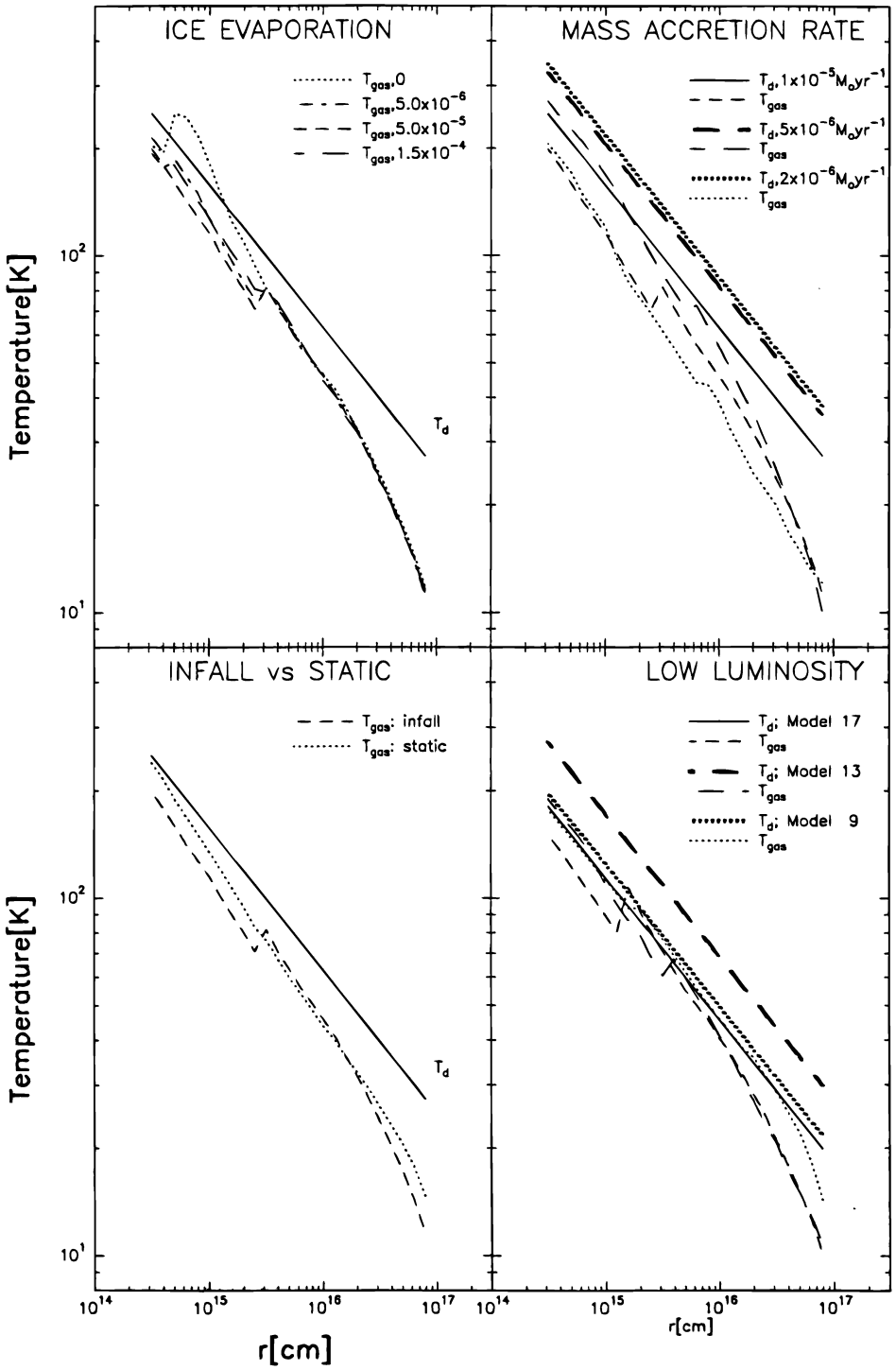

FIG. 5.—Gas and dust temperature profiles of the various models we considered for a 65 $L_\odot$ source and summarized in Table 3. *Top left:* Gas temperature profiles for different amounts of evaporated H_2O from grains (*dotted line*, no ice evaporation; *dashed line*, $x_{ice}(H_2O) = 5 \times 10^{-6}$; *dashed-dotted line*, $x_{ice}(H_2O) = 5 \times 10^{-5}$; standard model; *long-dashed line*, $x_{ice}(H_2O) = 1.5 \times 10^{-4}$; solid line represents the dust temperature profile). *Top right:* Dust and gas temperature profiles for different mass accretion rates (*solid and dashed lines*, dust and gas temperature for $\dot{M} = 10^{-5}\ M_\odot\ yr^{-1}$, i.e., standard model; *long-dashed lines*, dust and gas temperature for $\dot{M} = 5 \times 10^{-6}\ M_\odot\ yr^{-1}$; *dotted lines*, dust and gas temperature for $\dot{M} = 2 \times 10^{-6}\ M_\odot\ yr^{-1}$). *Bottom left:* Dust (*solid line*) and gas temperature profiles of our standard (collapsing envelope) model (*dashed line*) and the static envelope model (*dotted line*) described in the text. *Bottom right:* Dust and gas temperature profiles for the three models describing a 20 $L_\odot$ source: model 17, the "low-luminosity" case discussed in text, 1 $M_\odot$ and $\dot{M} = 10^{-5}\ M_\odot\ yr^{-1}$ and accretion luminosity reduced ad hoc by a factor of 3 (*solid and dashed lines*); model 13, 1 $M_\odot$ and $\dot{M} = 2 \times 10^{-6}\ M_\odot\ yr^{-1}$ (*long-dashed lines*); model 9, 0.16 $M_\odot$ and $\dot{M} = 10^{-5}\ M_\odot\ yr^{-1}$ (*dotted lines*).

The difference between the gas and dust temperature is larger for the highest luminosity. This is primarily due to the enhanced (optically thick) H_2O cooling in the 65 $L_\odot$ model, caused by the larger velocity fields (more massive protostar). Despite this difference, the main result is that the gas temperature in both cases is roughly equal to the dust temperature, and the more luminous model has slightly warmer gas. A smaller inner radius results in a higher

maximum temperature for the spherical infall region compared with the standard model.

5.2.2. *Ice Evaporation from Grains*

The effect of changing the amount of water evaporated from icy mantles of grains when $T_d \geq 100$ K is shown in the top left panel of Figure 5 for a 65 $L_\odot$ protostar. Only the inner region is affected by the change. In general, for lower amounts of ice evaporated, the gas temperature is higher because cooling decreases and the gas can become even warmer than the dust. For no evaporation at all (model 6), the gas is warmer than the dust in almost the entire inner region until the gas temperature exceeds 200 K and water is copiously formed by neutral gas phase reactions. The standard model represents a minimum in the gas temperature achieved as the ice abundance is varied. A factor of 3 increase (model 8) in the amount of water evaporated with respect to the standard model actually results in slightly warmer gas, as the increased number of water molecules does not increase the cooling rate significantly (most of the rotational cooling lines are optically thick) but does increase the rate of gas heating by NIR photopumping.

5.2.3. *Mass Accretion Rate*

The top right panel of Figure 5 shows the dust and gas temperature profiles for three values of $\dot{M}$ and $L_* = 65\ L_\odot$. The dust temperature can be understood by noting that in all three cases the Planck opacity of the dust at $r \gtrsim r_i \sim 3 \times 10^{14}$ cm is less than unity. Therefore, the dust is heated by the IR emission from the "dust photosphere" at $r \leq r_i$. The case $\dot{M} = 1 \times 10^{-5} M_\odot$ yr^{-1} ($M = 1\ M_\odot$, model 1) has considerably higher densities and opacities in the infall than the $\dot{M} = 2 \times 10^{-6}\ M_\odot$ yr^{-1} ($M = 3.24\ M_\odot$, model 5). Therefore, the former has a larger, cooler photosphere, which radiates 65 $L_\odot$ at longer wavelengths. At $r \geq r_i$, outside the photosphere, the dust is therefore cooler because of the reduced cross section for absorbing long-wavelength photons. The optically thicker envelope has warmer dust far inside the photosphere but cooler dust far outside the photosphere than its lower opacity counterpart.

In all cases, gas cooling in the outer region is dominated by the optically thick rotational line emission of CO; the main source of heating is compression for $r \gtrsim 3 \times 10^{15}$ cm (except for the very outer part in the standard model in which gas-grain collisions heat the gas more). In this region, both cooling and heating depend on the velocity field, so that the gas temperature is relatively independent of it and is roughly equal in all cases. In the inner parts, H_2O photopumping becomes important. The gas temperature tends to follow the dust temperature and hence tends to increase with decreasing $\dot{M}$. However, for the lowest $\dot{M}$ (and fixed luminosity), the increase in infall velocity causes such an increase in gas cooling that this trend reverses for $\dot{M} < 5 \times 10^{-6} M_\odot$ yr^{-1}.

5.2.4. *Static Envelope*

We compare the gas temperature profile of the static envelope model (model 18) with our standard model in the bottom left panel of Figure 5. The static envelope has a slightly warmer inner region because of higher line optical depths and therefore reduced cooling capacity of the gas. The main coolant is still the optically thick water rotational line emission, but the cooling rate is a factor 2.5 lower than in the standard model. The difference in the two gas temperature profiles decreases going outward, where the optical depths in cooling lines become more comparable in the two models.

5.2.5. *Low-Luminosity Model*

Model 17 represents an "interrupted accretion" case in which the accretion luminosity is reduced ad hoc to 0.3 of the standard model, although the central mass and all the other parameters are maintained equal. Physically, this model corresponds to an epoch in which the disk is accreting mass at a significantly higher rate than the central protostar, either because the disk mass is increasing or because a wind lifts material from the disk before it accretes onto the protostellar surface. Our "low-luminosity" model 17 has $L = 20\ L_\odot$, $\dot{M} = 1 \times 10^{-5}\ M_\odot$ yr^{-1}, and $M_* = 1\ M_\odot$. We compare this model with two models of equal luminosity in which the infall accretion rate is steady or "uninterrupted." Model 13 has a lower accretion rate, and model 9 has a smaller central mass. We show the dust and gas temperature profiles of the three models in the bottom right panel of Figure 5.

Model 13 has the same central mass and luminosity (1 $M_\odot$, 20 $L_\odot$) but has a lower accretion rate $\dot{M} = 2 \times 10^{-6}$ $M_\odot$ yr^{-1} consistent with uninterrupted flow. The gas temperature is similar in the outer region for models 13 and 17. The two temperature profiles start to differ when H_2O molecules become the main source of heating and cooling ($T_d \geq 100$ K). Gas with the lowest accretion rate becomes the warmest, as the dust temperature is warmer (see § 5.2.3). The gas temperature in model 13 becomes 25% warmer than the (high accretion) low-luminosity model 17.

Model 9 on the other hand, has the same accretion rate and luminosity as our low-luminosity model 17, but it has a central mass of 0.16 $M_\odot$, consistent with uninterrupted accretion. The lower central mass results in lower infall velocities, which increase the opacity in the cooling transitions and decrease the cooling efficiency. The net result is that model 9 has slightly (about 20%) warmer gas than model 17.

6. PREDICTED SPECTRA AND DIAGNOSTIC OF INFALL

6.1. *The Spectrum of the Standard Model*

In Figure 6 we show the (standard model) computed spectrum between 20 μm and 200 μm at a spectral resolving power of 10^4, approximately the resolution of the spectrometers on ISO. Fluxes are evaluated for a source at a distance of 160 pc. Table 4 reports the computed fluxes of the brightest [O I], CO, and H_2O lines. In Table 4 we evaluate the distance r_{max} at which the maximum contribution to the luminosity or observed flux in a line is produced. This is the value of r that gives the maximum of $r(dF/dr)$, where F is given by equation (24).

6.1.1. [O I] *Lines*

[O I] 63 μm is the brightest line. The [O I] flux-to-total FIR continuum flux ratio is about 3×10^{-5}, much lower than the values typical of photodissociation regions (PDRs) (10^{-2} to 10^{-3}) or shocked regions (10^{-1} to 10^{-2}). In contrast to PDRs and low-velocity shocks, [O I] 63 μm from infalling envelopes is the main coolant of the gas in a relatively small zone of the emitting region, and the gas heating mechanisms are quite different (in shocks and PDRs, the gas is in general considerably hotter than the dust). The plot of $r(dF_{line}/dr)$ for [O I] 63 μm is shown in Figure 7 as function of radius at different times. At all times the emis-

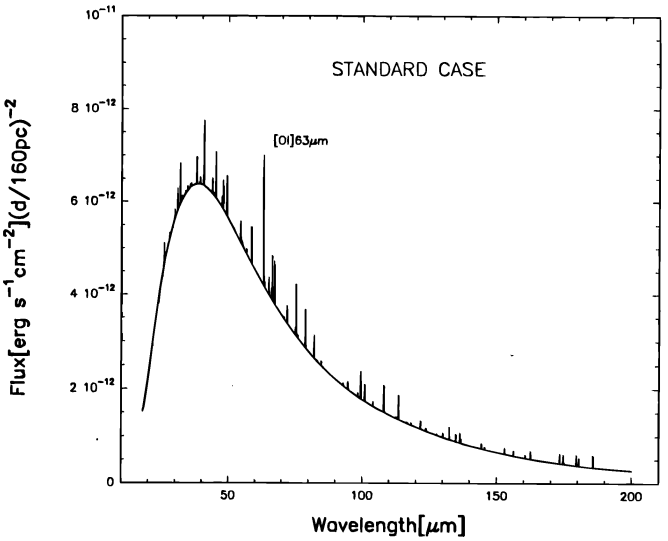

FIG. 6.—Line plus continuum spectrum between 20 μm and 200 μm of 1 $M_\odot$ protostar accreting at 10^{-5} $M_\odot$ yr^{-1} at 10^5 yr from the start of the collapse (our standard case), obtained with a resolution equal to 10^4. The continuum was obtained running the Wolfire & Cassinelli (1986) model.

sion originates in a region between about 2×10^{15} cm to 2×10^{16} cm. The inner radius is set by the sharp decrease of the atomic oxygen abundance in the warm gas close to the protostar, while beyond about 2×10^{16} cm the gas temperature is too low to excite the line ($T_{\rm gas} \leq 30$ K). [O I] 63 μm is (moderately) optically thick: the escape probability is about 0.4 ($t \geq 5 \times 10^4$ yr). The line luminosity depends weakly on the evolutionary time of the source, i.e., on its luminosity for 12.5 $L_\odot \leq L_* \leq 65$ $L_\odot$ and fixed $\dot{M}$. The optically thin [O I] 145 μm line is much less intense, ranging from 0.02 (at 10^5 yr) to 0.1 (at 10^4 yr) times the [O I] 63 μm line intensity.

6.1.2. CO *Lines*

The individual CO line luminosities peak at intermediate J transitions (Fig. 8) and are weaker than the [O I] 63 μm line. The brightest lines are around the $J = 8 \rightarrow 7$ transition, and most of these transitions are unobservable from the ground. The $J = 6 \rightarrow 5$ at 691 GHz lies in an atmospheric window and can be observed; we show the $r(dF_{\rm line}/dr)$ of this line in Figure 7 as a function of radius at different times. Most of the optically thick $J = 6 \rightarrow 5$ emission originates from the outer envelope. At 10^5 yr, it peaks at 6×10^{16} cm, where $n_{\rm H_2} = 9 \times 10^4$ cm^{-3}, $T_{\rm gas} = 14$ K, and $v = 0.2$ km s^{-1}. Note that although CO $J = 6 \rightarrow 5$ is locally optically thick, the observer still "sees" the inner regions because of the velocity shifts. Beyond the peak distance, the emission drops because of the dropping gas temperature.

The ratio of the CO total line luminosity-to-dust continuum luminosity is small, of order of 10^{-4}, and it reaches a maximum at 10^4 yr ($L_* = 12$ $L_\odot$) when it is 3×10^{-4}. Sensitive spectrometers with high spectral and spatial resolution are needed to detect the lines above the continuum. The proposed SOFIA will have such spectrometers. Unfortunately, CO lines in the ISO wavelength range are very weak and difficult to observe.

6.1.3. H_2O *Lines*

H_2O lines are numerous and bright and should be detectable by the ISO spectrometers. The brightest lines lie between 179 μm and 25 μm; the gas temperatures at $r > r_i$ are too small to excite the high energy levels that produce shorter wavelength transitions. Most lines are optically thick with escape probabilities less than 10^{-3} from their emitting regions. Of the 24 diagnostic lines listed in Table 4, only two lines ($4_{4,1} \rightarrow 4_{1,4}$ and $5_{4,1} \rightarrow 4_{1,4}$) have escape probability larger than 0.1 at their emission peaks. Although the self-absorption optical depths are high and the escape probabilities are low, some of the higher excitation lines and the lines produced in the lower density regions are from subthermally populated levels. Therefore, these lines are "effectively thin," in the sense that most collisional excitations ultimately result in the production of an escaping photon, after many self-absorbing scatterings. H_2O lines originate mostly in the regions in which water is very abundant, i.e., at radii less than about 4×10^{15} cm, and hence they have line widths of several km s^{-1}. Figure 7 shows the $r(dF_{\rm line}/dr)$ profile of some of the brightest lines.

Finally, the $6_{1,6} \rightarrow 5_{2,3}$ at 22 GHz has a population inversion in the inner region: we show the $r(dF_{\rm line}/dr)$ in Figure 7 as a function of time. It originates from $r \sim 4 \times 10^{14}$ cm, where water is abundant and warm, yet where the densities and radiation fields are sufficiently low to allow non-LTE level populations. The path lengths of greatest coherence, or the direction of maser beaming, is at $\mu^2 = \frac{2}{3}$ (see eq. [18]), or about 35° from the radial direction. We will discuss the water maser further in §§ 6.2.6 and 7.3.

6.2. *Diagnosing Physical Conditions from Line Spectra*

Table 5 reports the computed fluxes of the same lines as Table 4for each model. In the following we discuss how to use the line spectra to estimate the parameters of the model. We also discuss the spectra produced by the static envelope and the reduced luminosity models.

6.2.1. *Inner Radius*

Decreasing the inner radius increases the maximum temperature of the emitting gas. Since the [O I] and CO lines originate in the intermediate/outer regions, their fluxes are insensitive to this parameter. Water lines with upper level energies larger than 1000 K depend strongly on the value of r_i for $r_i \leq 3 \times 10^{14}$ cm. On the other hand, line fluxes of transitions with upper level energy levels less than about 400 K do not vary significantly. All the lines listed in Table 5 are at relatively low energy levels and therefore do not change appreciably when r_i decreases from 1×10^{14} cm to 3×10^{13} cm. Table 6 reports higher excitation lines, whose flux (from 160 pc) is higher than 10^{-12} ergs s^{-1} cm^{-2} when r_i is equal to 3×10^{13} cm and $L_* = 65$ $L_\odot$. These lines are particularly suitable for studying the hot component close to the central star. The 16.232 μm line flux (which rises by a factor of 4 as r_i varies from 1×10^{14} cm to 3×10^{13} cm) and the 22.639 μm line flux (which rises by a factor of 20 as r_i varies from 3×10^{14} cm to 1×10^{14} cm) are optimal choices to study r_i when $L_* = 65$ $L_\odot$. For lower luminosity sources, the 22.639 μm and 18.648 μm lines provide observable diagnostics. We note that these lines (FWHM $\sim$ 40 km s^{-1}) can be velocity resolved by the ISO spectrometers and hence can be probed for infall signature.

6.2.2. *Ice Evaporation from Grains*

In general, the [O I] and CO line fluxes are not affected by the ice content of grains. However, for a 65 $L_\odot$ source, CO line fluxes from $J_{\rm up} \geq 16$ are sensitive to H_2O evaporation from grains; with no evaporation, they increase more

TABLE 4

LINE FLUXES FOR THE STANDARD MODEL

λ (μm)	TRANSITION	FLUX (ergs s^{-1} cm^{-2})[a] 1×10^4 yr	5×10^4 yr	1×10^5 yr	r_{max} (cm)[b]	ϵ[c]
O I Lines						
145.601.....	$^3P_1 \rightarrow {}^3P_0$	2.1E−13	9.4E−14	5.8E−14	4.0E15	9.7E−1
63.101.....	$^3P_2 \rightarrow {}^3P_1$	2.4E−12	3.6E−12	2.8E−12	4.0E15	3.6E−1
CO Lines						
2600.76.....	$1 \rightarrow 0$	1.7E−14	2.2E−14	4.0E−14	1.0E17	1.3E−1
1300.38.....	$2 \rightarrow 1$	6.5E−14	1.0E−13	1.3E−13	1.0E17	2.9E−1
866.921.....	$3 \rightarrow 2$	9.6E−14	1.9E−13	1.7E−13	1.0E17	9.2E−1
650.191.....	$4 \rightarrow 3$	1.4E−13	2.9E−13	3.1E−13	7.9E16	1.4E−2
520.153.....	$5 \rightarrow 4$	2.2E−13	4.9E−13	4.8E−13	7.9E16	7.2E−2
433.461.....	$6 \rightarrow 5$	3.2E−13	7.3E−13	5.7E−13	6.3E16	1.1E−1
371.538.....	$7 \rightarrow 6$	3.8E−13	9.6E−13	5.7E−13	5.0E16	2.3E−1
325.095.....	$8 \rightarrow 7$	3.9E−13	1.0E−12	5.4E−13	3.2E16	1.7E−1
288.974.....	$9 \rightarrow 8$	3.9E−13	8.4E−13	5.0E−13	2.5E16	3.0E−1
260.076.....	$10 \rightarrow 9$	3.8E−13	6.5E−13	4.7E−13	1.6E16	2.3E−1
236.433.....	$11 \rightarrow 10$	3.7E−13	5.3E−13	4.3E−13	1.3E16	3.5E−1
216.730.....	$12 \rightarrow 11$	3.3E−13	3.6E−13	3.2E−13	6.3E15	2.1E−1
200.059.....	$13 \rightarrow 12$	3.1E−13	3.1E−13	2.9E−13	4.0E15	1.9E−1
185.769.....	$14 \rightarrow 13$	2.5E−13	2.7E−13	2.5E−13	4.0E15	4.0E−1
173.384.....	$15 \rightarrow 14$	1.9E−13	2.3E−13	2.0E−13	4.0E15	7.3E−1
162.548.....	$16 \rightarrow 15$	1.5E−13	1.8E−13	1.6E−13	1.3E15	4.0E−1
152.986.....	$17 \rightarrow 16$	1.2E−13	1.3E−13	1.3E−13	1.0E15	3.8E−1
144.487.....	$18 \rightarrow 17$	1.0E−13	1.0E−13	1.1E−13	7.9E14	4.3E−1
136.882.....	$19 \rightarrow 18$	8.3E−14	8.6E−14	1.0E−13	6.3E14	4.6E−1
130.038.....	$20 \rightarrow 19$	6.9E−14	7.1E−14	8.0E−14	5.0E14	4.7E−1
H_2O Lines						
179.527.....	$2_{1,2} \rightarrow 1_{0,1}$	5.6E−13	2.5E−13	2.2E−13	2.5E15	4.9E−5
113.538.....	$4_{1,4} \rightarrow 3_{0,3}$	1.8E−13	3.6E−13	5.0E−13	2.5E15	1.6E−4
108.073.....	$2_{2,1} \rightarrow 1_{1,0}$	3.6E−13	4.1E−13	5.6E−13	2.5E15	5.7E−5
100.913.....	$5_{1,4} \rightarrow 4_{2,3}$	1.1E−13	2.9E−13	3.5E−13	1.0E15	1.9E−3
99.493.....	$5_{0,5} \rightarrow 4_{1,4}$	1.3E−13	4.4E−13	5.6E−13	1.6E15	4.5E−4
82.032.....	$6_{1,6} \rightarrow 5_{0,5}$	1.8E−13	4.2E−13	4.8E−13	1.0E15	7.1E−4
78.742.....	$4_{2,3} \rightarrow 3_{1,2}$	2.1E−13	6.6E−13	8.1E−13	1.3E15	3.3E−4
75.381.....	$3_{2,1} \rightarrow 2_{1,2}$	3.0E−13	8.1E−13	1.1E−13	2.0E15	1.7E−4
71.947.....	$7_{0,7} \rightarrow 6_{1,6}$	2.2E−13	3.4E−13	3.8E−13	5.0E14	9.9E−4
67.269.....	$3_{3,0} \rightarrow 3_{0,3}$	2.7E−13	8.0E−13	9.2E−13	1.3E15	2.2E−2
66.438.....	$3_{3,0} \rightarrow 2_{2,1}$	2.8E−13	8.3E−13	9.7E−13	1.3E15	1.6E−4
65.166.....	$6_{2,5} \rightarrow 5_{1,4}$	2.5E−13	3.6E−13	3.7E−13	5.0E14	1.2E−3
58.699.....	$4_{3,2} \rightarrow 3_{2,1}$	3.5E−13	7.2E−13	7.9E−13	6.3E14	3.0E−4
54.507.....	$5_{3,2} \rightarrow 5_{0,5}$	3.4E−13	4.6E−13	4.5E−13	5.0E14	2.5E−2
49.391.....	$6_{3,4} \rightarrow 5_{2,3}$	3.2E−13	3.5E−13	3.4E−13	4.0E14	1.5E−3
49.337.....	$4_{4,1} \rightarrow 3_{3,0}$	4.1E−13	5.2E−13	5.2E−13	4.0E14	2.9E−4
47.973.....	$5_{3,2} \rightarrow 4_{2,3}$	4.3E−13	6.0E−13	6.2E−13	5.0E14	7.2E−4
45.112.....	$5_{2,3} \rightarrow 4_{1,4}$	5.1E−13	9.0E−13	9.8E−13	5.0E14	1.7E−3
43.894.....	$5_{4,1} \rightarrow 4_{3,2}$	3.7E−13	3.5E−13	3.2E−13	4.0E14	6.7E−4
40.691.....	$4_{3,2} \rightarrow 3_{0,3}$	5.8E−13	1.2E−12	1.4E−12	5.0E14	6.1E−3
37.984.....	$4_{4,1} \rightarrow 4_{1,4}$	5.7E−13	6.9E−13	5.8E−13	4.0E14	3.7E−1
31.772.....	$4_{4,1} \rightarrow 3_{1,2}$	6.7E−13	8.7E−13	8.5E−13	4.0E14	7.8E−2
30.899.....	$6_{3,4} \rightarrow 5_{0,5}$	5.3E−13	5.4E−13	4.6E−13	4.0E14	8.9E−3
25.940.....	$5_{4,1} \rightarrow 4_{1,4}$	5.6E−13	5.1E−13	4.3E−13	4.0E14	1.1E−1

[a] O I, CO, and H_2O line fluxes for a source of 1 $M_\odot$ accreting at 10^{-5} $M_\odot$ yr^{-1} at various times from the start of the collapse. The fluxes are computed for a source at 160 pc.

[b] r_{max} is the radius where most of the flux originates (see text).

[c] ϵ is the escape probability.

than a factor of 2 because of the sharp increase of the gas temperature in the inner region (see § 5.2.2).

Many H_2O lines are moderately sensitive to both r_i and the amount of water injected into the gas phase from the icy grain mantles when the dust temperature reaches 100 K. The 37.984 μm line (upper level energy about 700 K), which is effectively thin even in the dense inner regions, is very sensitive to ice evaporation without being sensitive to other parameters. The 31.772 μm line (same upper level) is also very sensitive to ice evaporation.

6.2.3. *Mass Accretion Rate*

The [O I] 63 μm line flux depends on the mass accretion rate, although not in a simple way. The [O I] 63 μm flux is shown in Figure 9 as function of $\dot{M}$ for 65 $L_\odot$ and 20 $L_\odot$ sources. For the parameter range studied, it is roughly constant for mass accretion rates between 5×10^{-6} $M_\odot$ yr^{-1} and 1×10^{-5} $M_\odot$ yr^{-1} almost independent of source luminosity. The line is moderately optically thick for mass accretion rates higher than about 5×10^{-6} $M_\odot$ yr^{-1}. In these

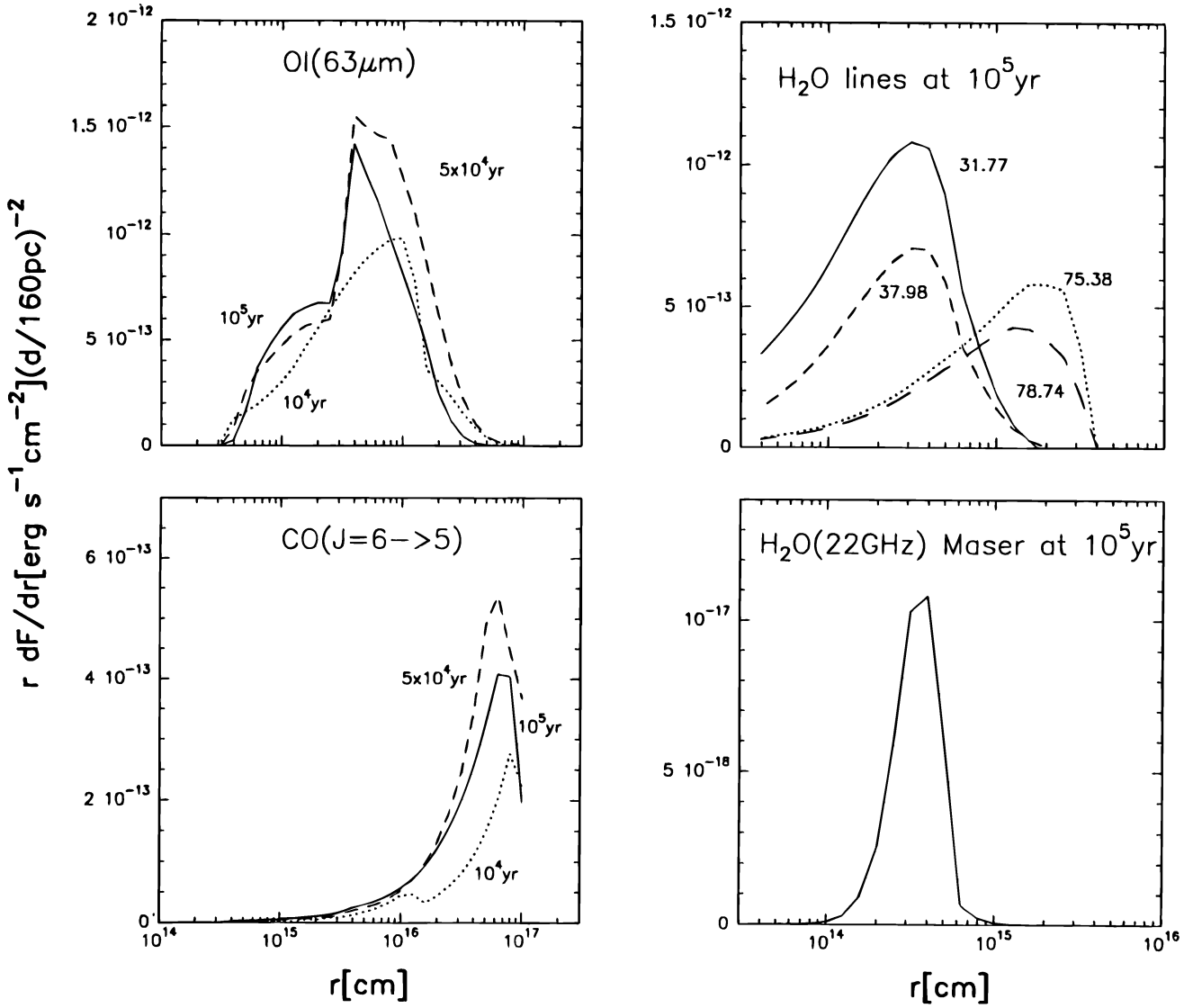

FIG. 7.—$r(dF_{line}/dr)$ vs. r of [O I] 63 μm line (*top left*), CO:6 → 5 line (*bottom left*) at 10^4 yr (*dotted lines*), 5×10^4 yr (*dashed lines*), and 10^5 yr (*solid lines*). Right panels show some H_2O bright lines (*top*) peaking at different radii and H_2O 22 GHz maser line (*bottom*) at 10^5 yr. Note that r in the right panels covers a reduced range. Fluxes are normalized for a source at 160 pc distance.

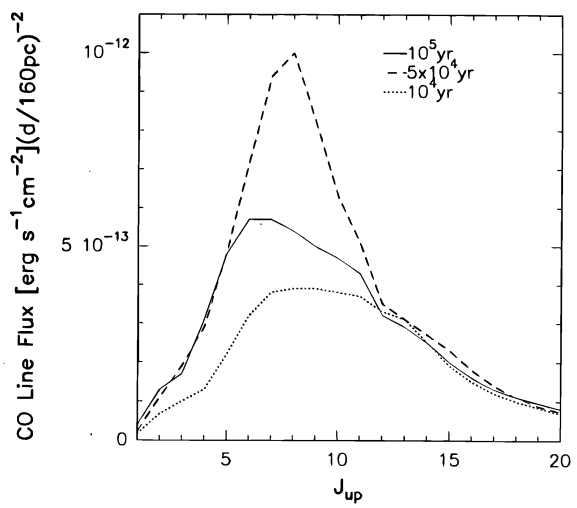

FIG. 8.—CO spectrum of a protostar accreting at $10^{-5}\ M_\odot\ \mathrm{yr}^{-1}$ at 10^4 yr (*dotted line*), 5×10^4 yr (*dashed line*), and 10^5 yr (*solid line*) from the start of the collapse. Fluxes are normalized for a source at 160 pc distance.

cases the [O I] 63 μm line originates mostly at $r \gtrsim 2 \times 10^{15}$ cm, at which the gas temperature profiles are approximately the same and are almost independent of the luminosity for the range considered. However, the [O I] 63 μm flux drops for smaller values of $\dot{M}$, for which the density of the envelope is low enough that the [O I] 63 μm line becomes optically thin. The line now traces a region closer to the center in which the temperature, velocity, and density profiles differ for different $\dot{M}$.

Figure 10 shows the CO line spectra for different values of the mass accretion rate. CO lines with $6 \leq J_{up} \leq 12$ are only moderately sensitive to the mass accretion rate (for fixed luminosity) because they are optically thick, and the peak emission arises from a region in which the gas temperature is somewhat less than $h\nu/k$ (for $J_{up} = 6$, for example, $T \leq 33$ K or $r \geq 3 \times 10^{16}$ cm). The radius of the "line photosphere" is only moderately sensitive to mass accretion rate for a given luminosity, since it depends as much on temperature as it does on gas density. CO lines would become optically thin for very low values of the mass

TABLE 5

LINE FLUXES FOR OTHER MODELS

	65 $L_\odot$								20 $L_\odot$								20 $L_\odot$	65 $L_\odot$
$\lambda(\mu m)$	1	2	3	4	5	6	7	8	9	10	11	12	13	14	15	16	17	18
O I Lines																		
145.601.....	0.5	0.5	0.5	0.3	0.0	0.9	0.6	0.6	2.0	2.0	2.0	0.9	0.0	2.2	2.0	2.1	0.4	0.6
63.101.....	27.	28.	28.	24.	1.1	42.	30.	32.	34.	34.	33.	33.	3.9	36.	34.	35.	22.	11.
CO Lines																		
2600.76.....	0.4	0.4	0.4	0.2	0.0	0.1	0.4	0.4	0.2	0.2	0.2	0.2	0.0	0.2	0.2	0.2	0.3	0.2
1300.38.....	1.3	1.3	1.3	0.6	0.3	0.7	1.2	1.2	0.7	0.7	0.7	0.6	0.2	0.7	0.7	0.7	0.9	0.8
866.921.....	1.7	1.8	1.7	1.6	0.9	1.8	1.6	1.7	1.1	1.1	1.1	1.1	0.6	1.1	1.1	1.1	1.3	1.1
650.191.....	3.1	3.1	3.1	3.0	1.6	3.3	3.0	3.1	1.6	1.6	1.6	2.0	1.2	1.6	1.6	1.6	2.3	1.3
520.153.....	4.8	4.8	4.8	4.3	2.0	4.9	4.7	4.9	2.7	2.7	2.7	3.4	1.7	2.7	2.7	2.7	3.5	2.2
433.461.....	5.7	5.7	5.7	5.1	2.0	5.9	5.5	5.8	4.0	4.0	4.0	4.9	1.9	4.0	4.0	4.0	3.9	3.1
371.538.....	5.7	5.7	5.7	5.6	2.0	6.1	5.7	5.8	5.0	5.1	5.1	6.2	2.0	5.0	5.1	5.0	3.9	3.4
325.095.....	5.4	5.4	5.4	6.0	1.9	5.9	5.4	5.5	5.4	5.5	5.5	7.3	2.1	5.5	5.4	5.5	3.7	3.0
288.974.....	5.0	5.0	4.9	6.1	1.7	5.6	5.0	5.2	5.7	5.7	5.8	7.7	2.0	5.6	5.6	5.6	3.5	2.4
260.076.....	4.7	4.7	4.7	6.2	1.5	5.3	4.7	5.0	5.7	5.9	5.9	6.4	1.9	5.7	5.7	5.7	3.3	2.0
236.433.....	4.3	4.3	4.3	5.9	1.3	5.0	4.3	4.5	5.8	5.8	5.8	4.6	1.6	5.8	5.8	5.8	3.0	1.6
216.730.....	3.2	3.2	3.2	4.7	1.1	3.8	3.3	3.4	4.6	4.6	4.6	2.9	1.1	4.6	4.6	4.6	2.3	0.9
200.059.....	2.9	2.9	2.9	4.1	0.9	3.7	3.0	3.2	3.5	3.5	3.5	2.5	0.9	3.6	3.5	3.5	2.1	0.8
185.769.....	2.5	2.5	2.6	3.7	0.8	3.6	2.7	2.9	2.7	2.7	2.7	2.1	0.8	2.8	2.7	2.8	1.9	0.7
173.384.....	2.0	2.1	2.2	3.4	0.7	3.5	2.3	2.5	2.2	2.3	2.3	1.8	0.7	2.3	2.2	2.2	1.6	0.6
162.548.....	1.6	1.7	1.8	3.2	0.6	3.4	1.9	2.1	1.8	2.0	2.0	1.6	0.6	1.9	1.8	1.6	1.3	0.6
152.986.....	1.3	1.4	1.5	3.0	0.5	3.3	1.6	1.8	1.5	1.6	1.7	1.4	0.5	1.6	1.5	1.4	1.0	0.5
144.487.....	1.1	1.3	1.4	2.8	0.4	3.2	1.5	1.6	1.2	1.4	1.4	1.3	0.4	1.4	1.2	1.2	0.6	0.5
136.882.....	1.0	1.2	1.3	2.6	0.3	3.1	1.3	1.4	0.9	1.1	1.1	1.2	0.3	1.2	1.0	1.0	0.4	0.4
130.038.....	0.8	1.0	1.2	2.2	0.2	3.0	1.2	1.2	0.7	0.9	0.9	1.1	0.2	1.1	0.8	0.8	0.3	0.4
H_2O Lines																		
179.527.....	2.2	2.3	2.9	6.6	3.1	1.4	2.8	3.0	7.4	7.4	7.4	3.5	1.9	7.4	7.4	7.4	1.6	1.3
113.538.....	5.0	5.4	5.6	15.	1.9	1.2	3.5	6.5	2.2	2.3	2.4	4.9	2.8	1.7	2.2	2.5	1.8	1.7
108.073.....	5.6	6.0	6.3	18.	3.3	1.4	4.5	7.1	4.0	4.1	4.2	5.4	3.9	3.5	4.0	4.3	2.2	1.9
100.913.....	3.5	4.0	4.4	8.5	0.4	0.8	1.6	6.1	1.9	2.1	2.2	4.1	1.2	0.3	1.4	2.5	1.4	1.6
99.493.....	5.6	6.0	6.5	15.	1.2	1.2	3.0	8.4	2.2	2.4	2.5	5.9	2.3	10.9	2.1	2.7	2.2	2.2
82.032.....	4.8	6.0	6.5	10.	0.4	1.4	2.4	9.0	3.0	3.4	3.5	6.3	1.3	0.5	2.2	4.0	2.1	2.4
78.742.....	8.1	9.0	9.9	19.	1.5	1.8	4.1	13.	3.5	3.9	4.0	8.9	3.0	1.1	3.1	4.4	3.2	3.4
75.381.....	11.	12.	13.	30.	3.0	2.3	6.9	15.	4.2	4.6	4.8	11.	5.3	2.2	4.1	5.2	4.0	3.8
71.947.....	3.8	5.6	6.1	8.7	0.1	1.4	1.8	7.8	3.0	3.5	3.7	5.4	0.6	0.2	1.6	4.8	1.4	2.1
67.269.....	9.2	11.	12.	19.	0.8	1.9	3.9	16.	4.6	5.2	5.4	11.	2.4	0.5	3.7	6.0	3.8	4.2
66.438.....	9.7	12.	13.	22.	1.5	2.2	4.6	16.	4.7	5.3	5.5	11.	3.1	0.9	3.9	6.1	4.1	4.3
65.166.....	3.7	5.6	6.5	7.0	0.0	1.3	1.7	7.8	3.3	3.9	4.2	5.4	0.5	0.2	1.8	5.4	1.3	2.3
58.699.....	7.9	10.	12.	14.	0.5	2.1	3.4	15.	5.4	6.2	6.5	9.6	1.5	0.6	3.6	7.5	3.2	4.2
54.507.....	4.5	7.6	8.9	7.6	0.0	1.3	1.7	10.	4.4	5.3	5.7	7.0	0.5	0.0	2.1	7.3	1.6	3.1
49.391.....	3.4	7.0	8.9	7.2	0.0	1.1	1.5	8.0	3.3	4.5	4.9	5.6	0.4	0.2	1.9	6.3	0.9	2.6
49.337.....	5.2	9.0	11.	8.8	0.3	1.6	2.2	12.	5.1	6.3	6.8	7.6	0.7	0.2	2.5	8.6	1.9	3.4
47.973.....	6.2	10.	12.	13.	0.2	2.0	2.6	14.	5.4	6.8	7.3	9.4	0.8	0.2	2.8	9.1	2.1	3.8
45.112.....	9.8	15.	17.	18.	0.3	3.1	4.2	21.	7.2	8.7	9.6	13.	1.4	0.4	4.2	11.	3.6	5.8
43.894.....	3.2	8.0	10.	5.4	0.1	1.0	1.3	8.5	3.8	5.4	6.3	5.7	0.3	0.0	1.7	7.5	0.8	2.7
40.691.....	14.	20.	23.	27.	0.5	4.1	5.9	27.	8.4	10.	11.	17.	2.3	0.4	5.6	13.	5.1	7.5
37.984.....	5.8	11.	15.	6.0	0.0	1.0	1.4	17.	6.7	9.0	10.	11.	0.2	0.0	2.1	12.	1.8	4.9
31.772.....	8.5	19.	24.	15.	0.0	2.8	3.3	22.	7.6	11.	13.	14.	0.5	0.0	3.9	14.	2.7	6.1
30.899.....	4.6	15.	21.	8.5	0.0	1.5	1.5	15.	4.9	8.2	10.	9.1	0.0	−0.2	2.5	11.	0.9	4.5
25.940.....	4.3	18.	26.	7.0	0.0	1.1	1.2	16.	4.2	9.4	13.	9.4	−0.1	−0.1	2.5	11.	0.8	4.6

NOTES.—Line fluxes, in units of 10^{-13} ergs s^{-1} cm^{-2} of the 18 models described in the text and reported in Table 3. The first eight models refer to a 65 $L_\odot$ source in which we varied all the parameters of the model with fixed luminosity, while runs 9–16 refer to a 20 $L_\odot$ source. Model 17 represents a 1 $M_\odot$ protostar at the end of the collapse in which the luminosity is 30% of the standard luminosity. Model 18 is the static envelope case (see text). Fluxes are computed for a source at 160 pc. The fluxes are reported as 0.0 if they are less than 10^{-14} ergs s^{-1} cm^{-2}.

accretion rates ($\leq 10^{-7}$ $M_\odot$ yr^{-1}, not considered in this work), and in that case, the lines would become much more sensitive to this parameter. We expect that the CO isotope lines are a better indicator of the mass accretion rate in the high accretion rate range.

However, in infalling gas the line width of the CO lines increases with J_{up}, since the higher transitions originate from the (warmer) inner regions in which the infall velocities are higher. Figure 11 shows how a measurement of the line width versus J_{up} could demonstrate the presence of infall and measure the central mass of the protostar. SOFIA or the Far Infrared Space Telescope (FIRST) should have the requested sensitivities and spectral resolution to perform such studies.

On average, H_2O lines are very weak for very low mass accretion rates ($\dot{M} \leq 2 \times 10^{-6}$ $M_\odot$ yr^{-1}), while they are very bright for $\dot{M} \geq 5 \times 10^{-6}$ $M_\odot$ yr^{-1} for both 65 $L_\odot$ and 20 $L_\odot$ sources. The low fluxes for low $\dot{M}$ are due to the decreased density of the envelope; although the lines are optically thick, they are typically subthermally populated

TABLE 6

FLUXES OF ADDITIONAL BRIGHT H_2O LINES

		$r_i = 3 \times 10^{14}$ cm		$r_i = 1 \times 10^{14}$ cm		$r_i = 3 \times 10^{13}$ cm	
$\lambda(\mu m)$	TRANSITION	20 $L_\odot$	65 $L_\odot$	20 $L_\odot$	65 $L_\odot$	20 $L_\odot$	65 $L_\odot$
34.549.....	$7_{3,4} \rightarrow 6_{2,5}$	0.2	0.9	0.4	0.7	0.6	1.2
32.313.....	$6_{4,3} \rightarrow 6_{1,6}$	0.2	0.1	0.5	0.8	0.7	1.3
23.895.....	$8_{4,5} \rightarrow 7_{1,6}$	−0.05	−0.05	0.2	0.4	0.6	1.3
23.817.....	$8_{3,6} \rightarrow 7_{0,7}$	−0.05	−0.08	0.4	0.8	0.8	1.6
22.639.....	$5_{5,0} \rightarrow 4_{2,3}$	0.2	0.07	0.7	1.3	1.1	2.3
22.620.....	$6_{5,2} \rightarrow 5_{2,3}$	0.01	−0.04	0.4	0.8	0.9	1.8
21.846.....	$9_{2,7} \rightarrow 8_{1,8}$	−0.1	−0.07	0.2	0.4	0.7	1.4
21.152.....	$8_{5,4} \rightarrow 7_{2,5}$	−0.06	−0.02	0.1	0.1	0.6	1.1
20.662.....	$7_{4,3} \rightarrow 6_{1,6}$	−0.04	−0.08	0.4	1.0	1.0	2.1
19.727.....	$7_{5,2} \rightarrow 6_{2,5}$	−0.1	−0.08	0.2	0.5	0.8	1.7
18.648.....	$6_{6,1} \rightarrow 5_{3,2}$	−0.04	−0.02	0.3	0.3	0.9	1.2
17.630.....	$7_{6,1} \rightarrow 6_{3,4}$	−0.05	−0.02	0.2	0.2	0.8	1.4
16.232.....	$9_{4,5} \rightarrow 8_{1,8}$	−0.03	−0.01	0.1	0.4	0.8	1.2

NOTE.—These lines are bright when the inner radius is 3×10^{13} cm. Fluxes are computed for a source at 160 pc and are in units of 10^{-12} ergs s^{-1} cm^{-2}.

and therefore effectively thin into quite small radii compared with the higher density cases. Therefore, the radius of their effective photosphere is quite dependent on the mass accretion rate. (Note that this does not apply to CO lines that are in thermal equilibrium.) H_2O lines with relatively low upper levels are sensitive to the mass accretion rate but relatively insensitive to either r_i or the amount of water evaporated from icy grains, since these lines in general become effectively optically thick at critical distances that lie beyond the evaporation region ($r \gtrsim 10^{15}$ cm). Their sensitivity to the mass accretion rate, however, is complicated. For example, the 75.381 μm line increases about a factor of 3 as the mass accretion rate decreases from 1×10^{-5} $M_\odot$ yr^{-1} to 5×10^{-6} $M_\odot$ yr^{-1}, and then it decreases by a factor of 4 as the mass accretion rates decreases further to 2×10^{-6} $M_\odot$ yr^{-1}. The higher line fluxes at $\dot{M} = 5 \times 10^{-6}$ $M_\odot$ yr^{-1} compared with the 10^{-5} $M_\odot$ yr^{-1} model are caused by the higher gas temperatures in the former model; in this case, the increase of the gas temperatures overwhelms the decrease of the density and the lines are brighter. The 78.742 μm line is also sensitive to the mass accretion rate and relatively insensitive to r_i and ice content. Although neither line increases monotonically with increasing mass accretion rate, their flux divided by the [O I] 63 μm flux is a good measure of $\dot{M}$. We show the 75.381 μm/63 μm and the 78.742 μm/63 μm ratios as functions of the mass accretion rate in Figure 12.

Figure 13 summarizes the parameter dependence of the six H_2O lines discussed above. All six lines are plotted against each parameter. The lines more suitable to estimate the particular parameter are marked with a star in the plot. However, we emphasize that these lines are only indicative and that a full modeling of all the lines is necessary to pin down the parameters.

6.2.4. *Outflow versus Infall*

Both observational and theoretical considerations indicate that outflows may occur simultaneously with infalls

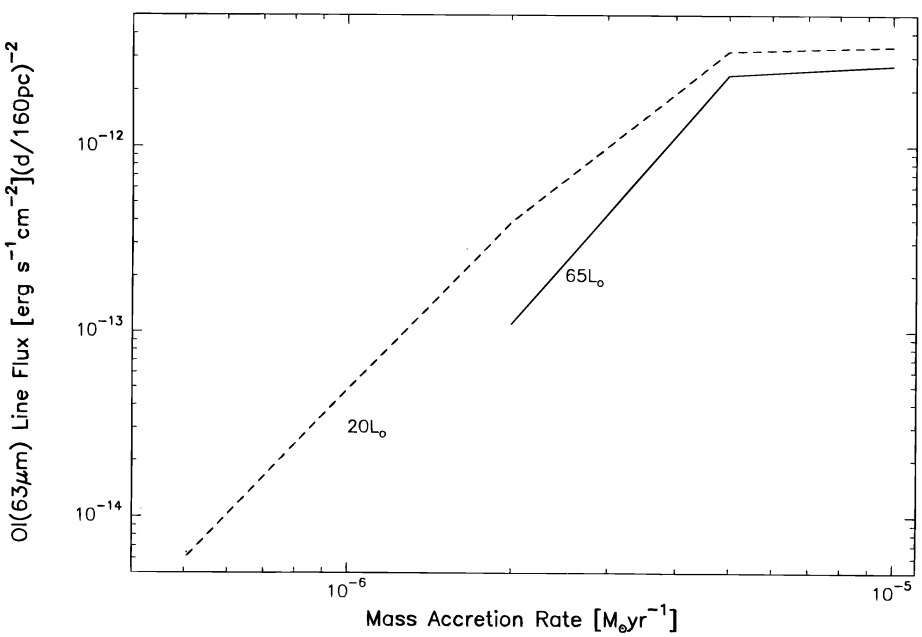

FIG. 9.—[O I] 63 μm line flux vs. the mass accretion rate for a 65 $L_\odot$ source (*solid line*) and for a 20 $L_\odot$ source (*dashed line*). Fluxes are normalized for a source at 160 pc distance.

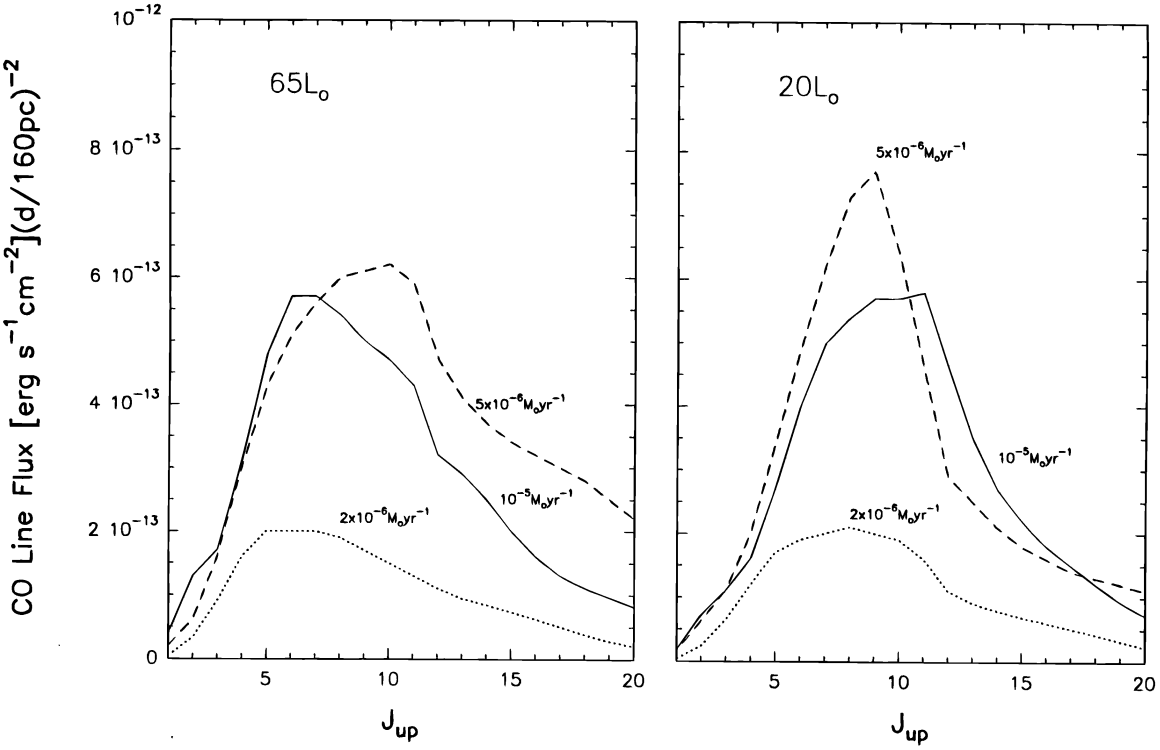

FIG. 10.—CO spectra vs. J_{up} of a 65 $L_\odot$ source (*left*) and a 20 $L_\odot$ source (*right*) for different values of the mass accretion rate: $10^{-5}\,M_\odot$ yr^{-1} (*solid lines*), $5 \times 10^{-6}\,M_\odot$ yr^{-1} (*dashed lines*), and $2 \times 10^{-6}\,M_\odot$ yr^{-1} (*dotted line*). Fluxes are normalized for a source at 160 pc distance.

(Shu et al. 1994a, 1994b). Therefore, warm shocked outflow gas might mimic or contaminate the spectrum from the warm infalling gas. The problem in identifying and removing this contamination is that, whereas the infall spectrum is defined quite uniquely by the tightly constrained density and temperature structure of the infalling gas, the shock spectrum is relatively unconstrained because of the wide range of possible preshock densities and velocities caused by the turbulence and unknown geometries and clumpiness of the shocked gas. Nevertheless, we can make a few general remarks. The warm infalling gas we have modeled is confined to regions close to the protostar and has relatively narrow line widths ($\leq$10 km s^{-1}) and unique line profiles (e.g., Zhou et al. 1993, or see Fig. 11). Spatially resolved lines

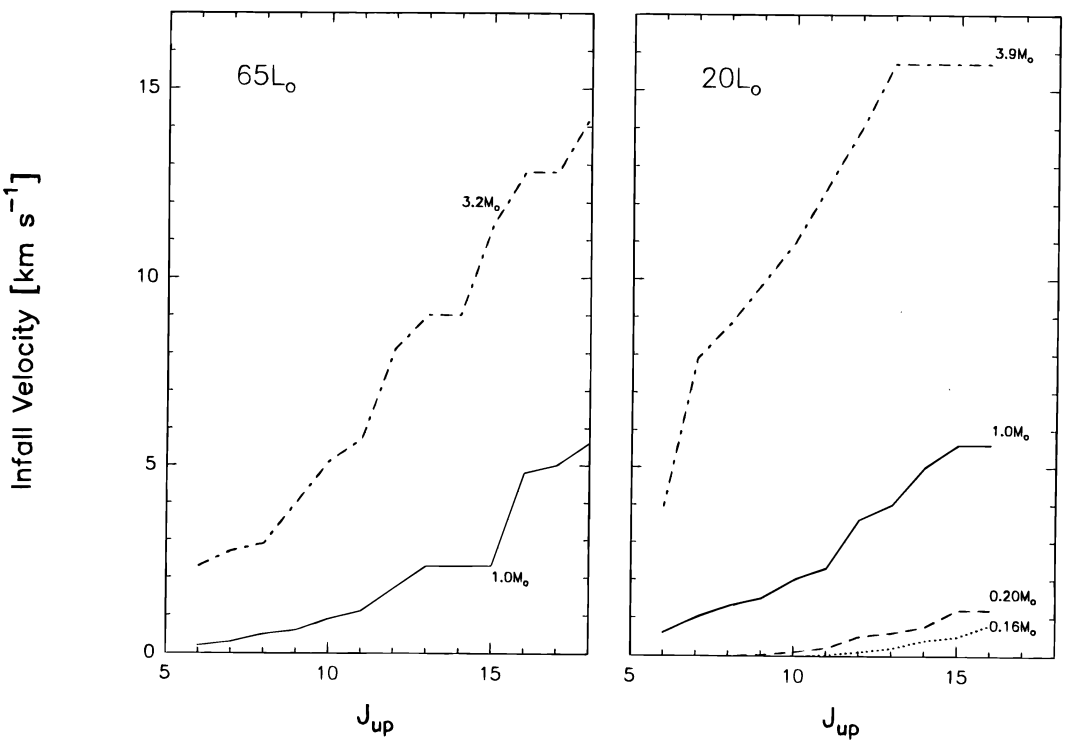

FIG. 11.—Infall velocity at the peak r_{max} of the CO line emission vs. J_{up} of a 65 $L_\odot$ source (*left*) and a 20 $L_\odot$ source (*right*) for different values of the central mass: 3.2 $M_\odot$ and 3.9 $M_\odot$ (*dash-dotted lines*), 1.0 $M_\odot$ (*solid lines*), 0.20 $M_\odot$ (*dashed line*), and 0.16 $M_\odot$ (*dotted line*).

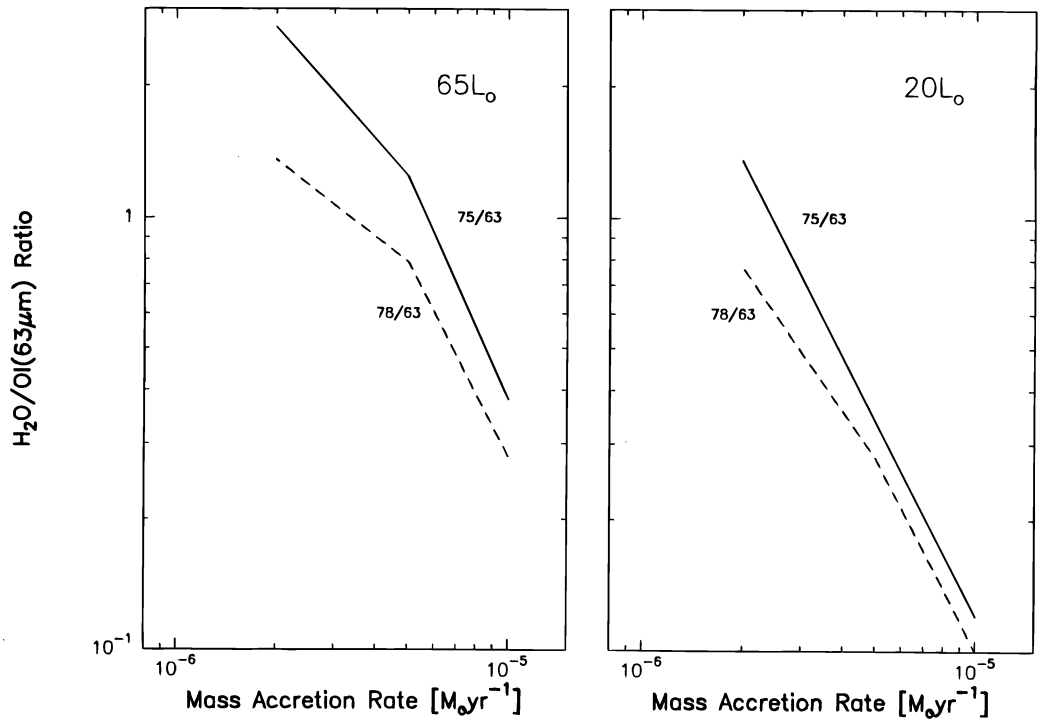

FIG. 12.—H_2O (75 μm)/[O I] 63 μm (*solid lines*) and H_2O (78 μm)/[O I] 63 μm (*dashed lines*) ratios vs. mass accretion rate of a 65 $L_\odot$ source (*left*) and a 20 $L_\odot$ source (*right*).

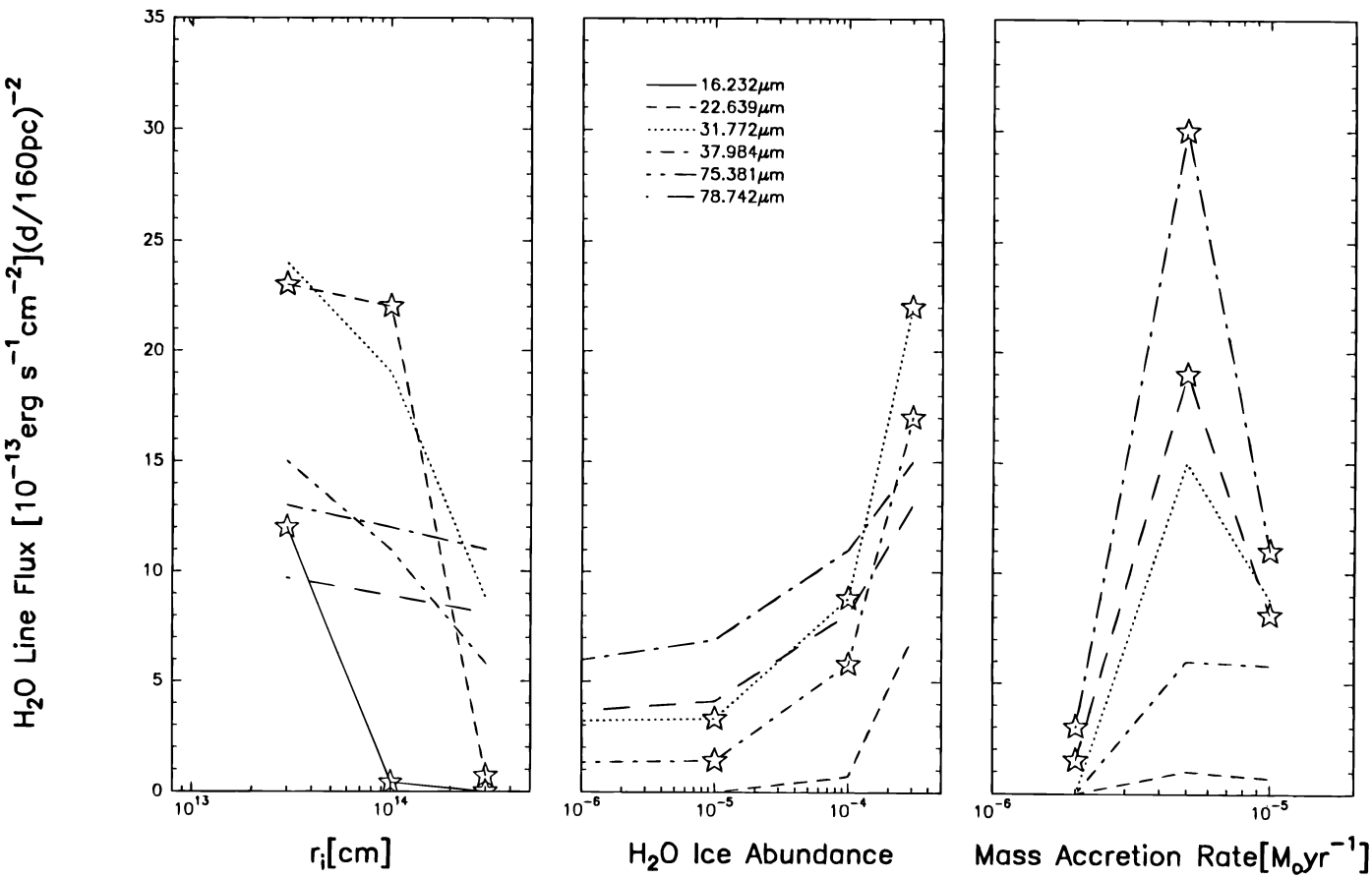

FIG. 13.—Six H_2O lines that can be used to estimate three key parameters of the model (see text). Optimum lines used to derive each parameter in the graph are marked by a star. Lines at 16.232 μm and 22.639 μm, with high upper level energy, are particularly sensitive to the inner radius r_i. Lines at 31.772 μm and 37.984 μm, with intermediate upper level energy, are appropriate to estimate the amount of water injected into the gas from the evaporation of grain ice. Lines at 75.381 μm and 78.742 μm can be used to estimate the mass accretion rate. Fluxes are normalized for a source at 160 pc distance.

with line widths greater than virial (i.e., gravitationally unbound) therefore likely to be produced in outflows. In addition, infalling gas has the characteristic that denser gas is warmer. For shocks, the reverse tends to be true: as gas cools in the postshock regions, it becomes denser. This may be especially evident in the H_2O spectrum. Comparing our infall H_2O spectra with the shock spectra of Kaufman & Neufeld (1996), we find that the infall far-infrared (FIR) spectra have brighter short-wavelength ($\lambda < 45$ μm) lines (from levels excited in denser warmer gas) relative to the longer wavelength lines than do the shock spectra.

6.2.5. *Static Envelope*

We have run a static envelope model with density and grain temperature profiles identical to the standard (infall) model, in order to find the strongest diagnostics of infall. With sufficient spectral resolution, the CO line width correlation shown in Figure 11 is clearly the strongest evidence. Lacking spectral or spatial resolution, however, line flux diagnostics are required. The largest difference in the line fluxes of the standard case and the static envelope case arises from H_2O lines that originate in the inner regions, in which the gas temperatures are higher in the static case (see § 5.2.4). Figure 14 shows the ratios between the flux obtained in the standard (infall) case divided by the flux of the static case for each line with flux (from 160 pc) larger than 3×10^{-13} ergs s^{-1} cm^{-2}, i.e., the 23 lines of Table 4. Because the ratios are not large ($\sim$2–3) and other parameters like ice evaporation can affect the H_2O fluxes, it will require careful modeling to find evidence for infall from line fluxes alone.

6.2.6. *Low-Luminosity Case*

Model 17 represents a "low-luminosity" case in which the accretion rate through the 10^{14}–10^{16} cm infall region is higher than the accretion rate onto the protostar. Therefore, the accretion luminosity is low relative to the mass infall rate outside r_i. Because there are differences in the density profile and minor differences in the temperature profile (see § 5.2.5), this case can be distinguished from models 9 and 13, which have the same 20 $L_\odot$ luminosity but which have steady accretion rates. The higher densities in model 17 compared to model 9 (with $\dot{M} = 2 \times 10^{-6}$ $M_\odot$ yr^{-1}) is diagnosed by the increased [O I] and, to a lesser extent,

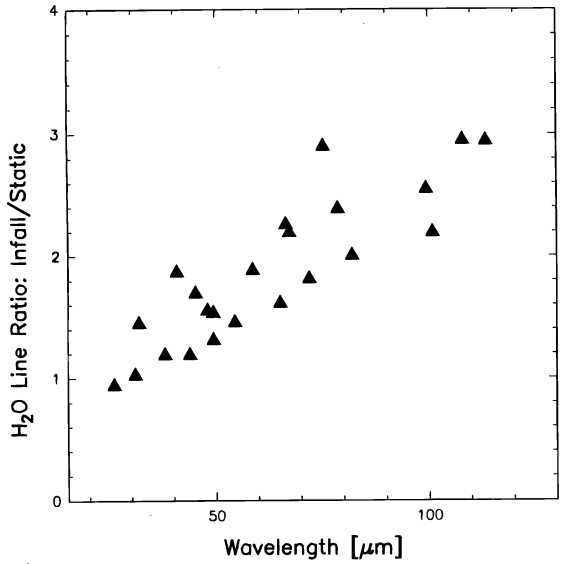

FIG. 14.—Ratio of H_2O line fluxes of the static case to the fluxes of the standard case vs. line wavelength.

H_2O line luminosities. The higher temperatures and densities in model 13 (with $M_* = 0.16$ $M_\odot$) leads to stronger H_2O and [O I] lines in general than in model 17.

6.2.7. H_2O 22 GHz *Maser*

The $6_{1,6} \rightarrow 5_{2,3}$ transition, whose upper level energy is about 600 K above the ground state, has a population inversion and produces a flux (from 160 pc) of about 10^{-17} ergs s^{-1} cm^{-2} in the standard 65 $L_\odot$ case. Table 7 gives the predicted flux, the region r_{max} in which the peak emission originates, and the infall velocity at that point for each model. Table 7 shows that the maser luminosity is much higher for the 65 $L_\odot$ case than for the 20 $L_\odot$ case. It shows also that for a fixed protostellar luminosity, the maser luminosity depends mainly on the mass accretion rate (i.e., the gas density and temperature) and the water abundance. For a fixed protostellar luminosity of either 20 or 65 $L_\odot$, the maser luminosity peaks for $\dot{M} \sim 5 \times 10^{-6}$ $M_\odot$ yr^{-1} (see models 3–5 and models 11–13) due to the high gas temperatures in the inner regions compared with higher mass accretion rates and to the high gas densities in the inner

TABLE 7

H_2O 22 GHz MASER LINE

Model	Flux (10^{-18} ergs s^{-1} cm^{-2})	r_{max} (10^{14} cm)	v (km s^{-1})
1.....	11	4	8
2.....	11	4	8
3.....	11	4	8
4.....	23	4	9
5.....	$\leq 10^{-3}$	...	...
6.....	0.02	4	8
7.....	0.03	4	8
8.....	320	6	6
9.....	0.2	6	3
10.....	0.2	6	3
11.....	0.2	6	3
12.....	2	6	3
13.....	0.01	6	6
14.....	$\leq 10^{-3}$	...	...
15.....	0.005	6	3
16.....	3	13	2
17.....	0.06	4	8

NOTE.—Fluxes are computed for a source at 160 pc.

regions compared with lower mass accretion rates. Models 8 and 16, which have the maximum ice evaporated, produce the strongest masers for the two luminosities. The line comes from rather close ($r_{max} \sim 4 \times 10^{14}$ cm) to the central object, and it traces a region in which the infall velocity is about 8 km s^{-1} (65 $L_\odot$) or 3 km s^{-1} (20 $L_\odot$). The maser is beamed in the direction $\mu = (\frac{2}{3})^{1/2} = 0.82$ (see eq. [18]), or about 35° from the radial direction. Thus, the observer should see two velocity components, one redshifted and one blueshifted by 0.82 times the infall velocity at r_{max}. For sources with $L > 20\ L_\odot$, the masing fluxes are potentially observable from large, ground-based telescopes.

7. OBSERVATIONAL CONSTRAINTS

7.1. [O I] 63 μm *Line*

Few observations of the [O I] 63 μm line toward young stellar objects (YSOs) have been reported. Cohen et al. (1988) detected a signal of 5–15 $\times 10^{-12}$ ergs s^{-1} cm^{-2} from T Tau, L1551−IRS 5, and DG Tau in a beam of 33″–44″. Ceccarelli et al. (1996) reported a flux of about 6×10^{-12} ergs s^{-1} cm^{-2} toward VLA 1623, IRAS 16293−2422, L1448C, and NGC 1333-IRAS 4. The line widths have not been resolved, and the line fluxes have been attributed to shock emission, mainly because of the presence of observed outflows from these sources. The origin of this line emission is difficult to establish until higher spectral resolution is available with, for example, SOFIA. Nevertheless, the observed fluxes are consistent with the predictions of a number of our models, and therefore a significant part of the observed fluxes could be due to the collapsing envelopes surrounding these objects.

7.2. CO $J = 6 \rightarrow 5$ *Line*

Schuster et al. (1993) report observations of CO $J = 6 \rightarrow 5$ line emission from three T Tauri stars. They observed a line flux of about 4–8 $\times 10^{-14}$ ergs s^{-1} cm^{-2} with an FHWM of 5 km s^{-1} in T Tau and HL Tau extending about 15″ in diameter ($=3 \times 10^{16}$ cm at 160 pc distance) and 2 km s^{-1} in GG Tau over a 25″ region. The lines show also a broader component in the blue wing, probably originating in the wind shock. These stars are known from their luminosities to have mass accretion rates onto the protostellar surfaces lower than about 5×10^{-7} $M_\odot$ yr^{-1} (Bertout & Basri 1989; Hartmann & Kenyon 1990), so our model is not directly applicable to these sources unless the infall accretion onto the protostellar disks is much higher.

We ran a model with a very low mass accretion rate, $\dot{M} = 5 \times 10^{-7}\ M_\odot$ yr^{-1}, and a source luminosity of 20 $L_\odot$, in order to have a rough but more reliable comparison between our model and these observations. Our model gives CO $J = 6 \rightarrow 5$ line emission peaked around 6×10^{15} cm, with significant emission arising from larger radii, and with a flux of 2.5×10^{-14} ergs s^{-1} cm^{-2} at 160 pc. Both predicted line flux and the spatial extent are consistent with the observations. Therefore, a rough comparison seems to attribute at least a part of the observed signal to the collapsing envelope emission.

7.3. H_2O 22 GHz *Maser*

A recent survey of H_2O 22 GHz maser emission toward 42 sources with luminosities less than 120 $L_\odot$ was carried out by Wilking et al. (1994). They found that all sources with $L \geq 25\ L_\odot$ display maser activity and that the emission is variable in time. A total of 20 sources show maser emission; the luminosity in the maser line ranges between less than 10^{-10} to 10^{-6} of the source luminosity, with most at the lower end of the range. In our standard model, this ratio is equal to 10^{-10}. With fixed luminosity, the ratio increases for either a higher water abundance in the innermost region or for a somewhat lower mass accretion rate. Small and variable departures in spherical symmetry could produce asymmetric and variable beaming and explain the time variability and the larger (apparent) isotropic luminosities observed in some cases.

Our parameter study is insufficient to probe the maser emission fully, and that is not the main focus of this paper, but we emphasize that the available data do not always definitively indicate an outflow or shock origin. Spatial maps and detailed spectra have been published only for a few cases (Terebey, Vogel, & Myers 1992; Wootten 1989), and they have been used to infer that the line originates in low-velocity shocks (outflow). However, there are only three mapped sources. In one case (IRAS 16293−2422), the highest velocity component (14 km s^{-1}) in the wing of an emission spot (that also has the *lowest brightness* in the line) is used to conclude that the velocities indicate outflow and not infall. However, most of the maser emission comes from gas at ≤ 4 km s^{-1}, fully consistent with collapsing gas. Moreover, the highest velocity component may reflect the binary nature of the source (Wootten 1989). In a second source (IRAS 05417+0907) Terebey et al. (1992) conclude that the uncertainty in the relative positions does not allow one to infer whether the gas is infalling or outflowing. Only in the faintest of the three sources, YLW 16A (a more evolved object with a weak outflow; André & Montmerle 1994; Saraceno et al. 1996), does the maser emission originate unambiguously in gravitationally unbound gas.

8. SUMMARY AND CONCLUSIONS

The main thrust of this paper has been to calculate the evolution of the gas temperature and the line spectrum in a spherical envelope of gas and dust infalling onto a moderately luminous (20–65 $L_\odot$ at $t = 10^5$ yr), low-mass (0.1–1 $M_\odot$ at 10^5 yr) protostar. We have focused on the regions $r \sim 10^{16}$–10^{14} cm from the star. These regions are inside regions generally studied at radio and millimeter wavelengths, but outside the centrifugal radius at which departures from spherical symmetry become important. These regions have gas and dust temperatures of ~30–300 K and infall velocities of ~1–10 km s^{-1} at evolution times of 10^5 yr. The main result is that the gas temperature follows the dust temperature closely, rising with decreasing r.

Our model self-consistently includes the dynamics, chemistry, heating and cooling, and radiative transfer in the infalling gas and dust. We have used the Shu (1977) "inside out" collapse model and time-dependent chemistry including 44 species. Our thermal balance calculation featured coupling of the gas to dust IR photons, collisional heat transfer of gas and dust at different temperatures, compressional heating in the infall, and radiative cooling primarily by [O I] 63 μm and CO and H_2O rotational transitions. An escape probability formalism was utilized to calculate emergent line fluxes and local cooling rates.

We have found that the chemistry that determines the abundances of the dominant coolants is particularly simple. Essentially all gas-phase carbon remains incorporated in CO in the infall. Gas-phase oxygen not incorporated in CO

is mostly in O and O_2, at a relatively constant ratio, until the gas and dust fall close enough to the protostar to warm the dust to about 100 K. At this point, H_2O ice evaporates from the grains and injects all of the ice mantle into the gas phase. As infall proceeds further, the gas warms to greater than 200 K and gas-phase reactions drive O and O_2 into H_2O.

In the inner regions ($r < 3 \times 10^{15}$ cm), the gas is heated by the (CO and H_2O) absorption of NIR photons from warm dust located even closer to the protostar. The cooling is mainly by H_2O rotational lines. Masing of the 22 GHz H_2O line occurs in the inner regions. In the outer regions ($r > 10^{16}$–10^{17} cm), the gas is heated by collisions with (warmer) dust grains and is cooled by CO rotational lines. In the intermediate regions, the gas is heated mainly by compressional heating and cooled by [O I] 63 μm and CO rotational lines.

The infrared lines of [O I], H_2O, and CO are observable and diagnostic of the physical conditions in the collapse. The spectra probe several physical parameters: the mass infall rate (at $r \sim 10^{14}$–10^{16} cm), the amount of H_2O ice present on the infalling grains, and the inner (centrifugal) radius. Infall versus static envelopes are hardly distinguished by line fluxes only: however, we show that the line widths of the CO rotational lines as a function of J provide the best evidence for infall, that the [O I] 63 μm flux and the ratio of H_2O (75.381 or 78.742 μm) to [O I] 63 μm are sensitive to the mass infall rate, that the H_2O (37.984 and 31.772 μm) lines probe the amount of H_2O ice evaporated from the grains, and that several high-excitation H_2O lines (e.g., 16.232, 18.648, and 22.639 μm) probe the inner radius.

Recent and planned advances in infrared astronomy make the detection of these spectral lines possible. The H_2O lines and the [O I] 63 μm line will be detectable by the spectrometers on board ISO. The [O I] 63 μm and the mid-J ($J \sim 7$–15) CO lines can be detected and spectrally resolved by SOFIA. Finally, a few mid-J CO lines (e.g., $J = 6$–5) can be detected by ground-based submillimeter telescopes.

We thank R. Friedman for the help in using the HITRAN database, M. Wolfire for providing us with his code to compute the dust continuum, and M. Kaufman for running the code. It is a pleasure to thank our referee, S. Stahler, for his very useful comments that helped to make clearer the text. D. J. H. would like to acknowledge NASA RTOP 399-20-10, which supports the Center for Star Formation Studies, a consortium of researchers from NASA Ames Research Center, the University of California at Berkeley, and the University of California at Santa Cruz. Some of the computations presented in this paper were performed at the Centre de Calcul de l'Observatoire de Grenoble.

APPENDIX A

CHEMISTRY

We considered the following 44 species: H, H^+, He, He^+, C, C^+, O, O^+, Si, Si^+, S, S^+, Mg, Mg^+, Fe, Fe^+, H_2, H_2^+, CH, OH, SiH, CO, O_2, SiO, CH_2, H_2O, CH^+, OH^+, CO^+, SiO^+, H_3^+, CH_2^+, H_2O^+, SiH_2^+, HCO^+, $HOSi^+$, CH_3^+, H_3O^+, e, H^-, PAH, PAH^-, PAH^+, and $PAHH^+$. Our chemical network consists of 182 reactions between those species. We adopted the reaction rates reported in Tielens & Hollenbach (1985), with the exceptions noted in Table 8.

PAHs, in neutral, anionic, and cationic form as well as protonated PAHs, $PAHH^+$, play a key role in the degree of ionization of dense clouds (Omont 1986; Lepp & Dalgarno 1988). PAH^- is formed by the attachment of electrons to neutral

TABLE 8

MOLECULAR IONS CHARGE EXCHANGE REACTIONS

Reaction	a
$H_3^+ + Mg \rightarrow Mg^+ + H_2 + H$.....	1.0×10^{-9}
$H_3^+ + Fe \rightarrow Fe^+ + H_2 + H$.....	4.9×10^{-9}
$CH^+ + Mg \rightarrow Mg^+ + CH$.....	3.6×10^{-10}
$CH^+ + Si \rightarrow Si^+ + CH$	2.0×10^{-10}
$CH^+ + S \rightarrow S^+ + CH$.....	4.7×10^{-10}
$CH^+ + Fe \rightarrow Fe^+ + CH$.....	2.6×10^{-10}
$O^+ + Fe \rightarrow Fe^+ + O$.....	2.9×10^{-9}
$OH^+ + S \rightarrow S^+ + OH$	4.3×10^{-10}
$H_2O^+ + Mg \rightarrow Mg^+ + H_2O$.....	2.2×10^{-9}
$H_2O^+ + Si \rightarrow Si^+ + H_2O$	3.0×10^{-9}
$H_2O^+ + S \rightarrow S^+ + H_2O$.....	4.3×10^{-10}
$H_2O^+ + Fe \rightarrow Fe^+ + H_2O$	1.5×10^{-10}
$SiO^+ + Mg \rightarrow Mg^+ + SiO$	1.0×10^{-9}
$SiO^+ + Fe \rightarrow Fe^+ + SiO$	1.0×10^{-9}

NOTE.—We adopted the reaction rates reported in Tielens & Hollenbach 1985 with the following exceptions: (1) We did not consider photodissociation reactions and reactions of vibrationally excited hydrogen. (2) We used the updated values to some reaction coefficients following Hollenbach, Takahashi, & Tielens 1991 (their Table 1). (3) We added the reactions reported in this table of molecular ion charge exchange, where the rates are taken from Millar et al. 1991. (4) We updated rates of the reactions with an activation barrier following Wagner & Graff 1987.

PAHs, with a rate coefficient of $1.2 \times 10^{-7} N_C^{3/4} S(e)$ cm^3 s^{-1}, where N_C is the number of carbon atoms (Allamandola, Tielens, & Barker 1989). In this work, we considered PAHs with 50 carbon atoms. The electron sticking coefficient $S(e)$ depends on the number of carbon atoms in the PAH, and $S(e) \sim 1$ for PAHs with 30 carbon atoms or larger (Tielens 1993). PAH^- is neutralized by recombination with metal and molecular ions and has a rate coefficient of $8 \times 10^{-8} N_C^{1/2} (T_{gas}/10\ \mathrm{K})^{-1/2}$ cm^3 s^{-1} (Draine & Sutin 1987). PAH^+ is formed by charge exchange of neutral PAHs with atomic ions and has an estimated rate coefficient of $5.5 \times 10^{-10} N_C^{1/2}$ cm^3 s^{-1}. $PAHH^+$ is formed by proton exchange of XH^+ ions with neutral PAHs, i.e., by the reactions

$$\mathrm{PAH} + \mathrm{XH}^+ \rightarrow \mathrm{PAHH}^+ + \mathrm{X}\ ,$$

with rate coefficients assumed to be $5.5 \times 10^{-10} N_C^{1/2}$ cm^3 s^{-1}. Both PAH^+ and $PAHH^+$ are neutralized by recombination with electrons or PAH^- with rate coefficients of $5.9 \times 10^{-5} N_C^{1/2} T_{gas}^{-1/2}$ cm^3 s^{-1} and $5.6 \times 10^{-7} T_{gas}^{-1/2}$ cm^3 s^{-1}, respectively. Finally, we adopted a PAH abundance per H nucleus equal to 1×10^{-7}, which is consistent with the fact that about 5% of the IR emission is emitted in the IR emission features (Tielens 1993). The reactions involving PAHs are reported in Table 9. Reaction rates in Tables 8 and 9 have the format

$$k = a\left(\frac{T}{300\ \mathrm{K}}\right)^b \mathrm{cm}^3\ \mathrm{s}^{-1}\ .$$

For reactions involving neutral PAHs, rates have been estimated following Allamandola et al. (1989) using a polarizability of $1.5 \times 10^{-24} N_C$, derived by fitting experimental measurements on small PAHs. We note that approximating PAHs by infinitesimally thin, circular disks and using electrostatics leads to a somewhat different dependence of the reaction rate coefficients on N_C (i.e., $\propto N_C^{3/4}$ rather than $\propto N_C^{1/2}$), corresponding to a polarizability dependence of $N_C^{3/2}$. For $N_C = 50$, the two approximations differ by less than 10%. The theoretical rate coefficients are in reasonable agreement with experimental studies on the charge exchange between C^+ and Xe^+ with benzene and naphthalene (Abouelaziz et al. 1993). Measured

TABLE 9

PAH REACTIONS

Reaction	a	b
$PAH + e \rightarrow PAH^-$	8.5×10^{-7}	0
$PAH^- + H^+ \rightarrow PAH + H$	1.0×10^{-7}	−0.5
$PAH^- + He^+ \rightarrow PAH + He$	1.0×10^{-7}	−0.5
$PAH^- + C^+ \rightarrow PAH + C$	1.0×10^{-7}	−0.5
$PAH^- + O^+ \rightarrow PAH + O$	1.0×10^{-7}	−0.5
$PAH^- + Si^+ \rightarrow PAH + Si$	1.0×10^{-7}	−0.5
$PAH^- + S^+ \rightarrow PAH + S$	1.0×10^{-7}	−0.5
$PAH^- + Mg^+ \rightarrow PAH + Mg$	1.0×10^{-7}	−0.5
$PAH^- + Fe^+ \rightarrow PAH + Fe$	1.0×10^{-7}	−0.5
$PAH^- + H_2^+ \rightarrow PAH + H + H$	1.0×10^{-7}	−0.5
$PAH^- + CH^+ \rightarrow PAH + C + H$	1.0×10^{-7}	−0.5
$PAH^- + OH^+ \rightarrow PAH + O + H$	1.0×10^{-7}	−0.5
$PAH^- + CO^+ \rightarrow PAH + C + O$	1.0×10^{-7}	−0.5
$PAH^- + SiO^+ \rightarrow PAH + Si + O$	1.0×10^{-7}	−0.5
$PAH^- + H_3^+ \rightarrow PAH + H_2 + H$	1.0×10^{-7}	−0.5
$PAH^- + CH_2^+ \rightarrow PAH + CH + H$	1.0×10^{-7}	−0.5
$PAH^- + CH_2^+ \rightarrow PAH + H_2 + C$	1.0×10^{-7}	−0.5
$PAH^- + H_2O^+ \rightarrow PAH + OH + H$	1.0×10^{-7}	−0.5
$PAH^- + H_2O^+ \rightarrow PAH + H_2 + O$	1.0×10^{-7}	−0.5
$PAH^- + SiH_2^+ \rightarrow PAH + SiH + H$	1.0×10^{-7}	−0.5
$PAH^- + HCO^+ \rightarrow PAH + CO + H$	1.0×10^{-7}	−0.5
$PAH^- + HOSi^+ \rightarrow PAH + SiO + H$	1.0×10^{-7}	−0.5
$PAH^- + HOSi^+ \rightarrow PAH + OH + Si$	1.0×10^{-7}	−0.5
$PAH^- + CH_3^+ \rightarrow PAH + CH_2 + H$	1.0×10^{-7}	−0.5
$PAH^- + H_3O^+ \rightarrow PAH + H_2O + H$	1.0×10^{-7}	−0.5
$PAH^- + H_3O^+ \rightarrow PAH + OH + H$	1.0×10^{-7}	−0.5
$PAH + HCO^+ \rightarrow PAHH^+ + CO$	3.9×10^{-9}	0
$PAH + H_3O^+ \rightarrow PAHH^+ + H_2O$	3.9×10^{-9}	0
$PAH + H_3^+ \rightarrow PAHH^+ + H_2$	3.9×10^{-9}	0
$PAH + CH_3^+ \rightarrow PAHH^+ + CH_2$	3.9×10^{-9}	0
$PAH + H^+ \rightarrow PAH^+ + H$	3.9×10^{-9}	0
$PAH + He^+ \rightarrow PAH^+ + He$	3.9×10^{-9}	0
$PAH + C^+ \rightarrow PAH^+ + C$	3.9×10^{-9}	0
$PAH + O^+ \rightarrow PAH^+ + O$	3.9×10^{-9}	0
$PAH + Si^+ \rightarrow PAH^+ + Si$	3.9×10^{-9}	0
$PAH + S^+ \rightarrow PAH^+ + S$	3.9×10^{-9}	0
$PAH + Mg^+ \rightarrow PAH^+ + Mg$	3.9×10^{-9}	0
$PAH + Fe^+ \rightarrow PAH^+ + Fe$	3.9×10^{-9}	0
$PAH^+ + PAH^- \rightarrow PAH + PAH$	3.2×10^{-8}	−0.5
$PAHH^+ + PAH^- \rightarrow PAH + PAH + H$	3.2×10^{-8}	−0.5
$PAHH^+ + e \rightarrow PAH + H$	2.4×10^{-5}	−0.5
$PAH^+ + e \rightarrow PAH + H$	2.4×10^{-5}	−0.5

electron recombination rates for small PAH cations ($N_C < 10$) (Abouelaziz et al. 1993) are much smaller than the electron capture rates adopted here. However, the efficiency with which the recombination energy is dispersed through the vibrational modes of the PAH increases exponentially with N_C, and therefore the adopted recombination rate coefficients are likely reasonable for $N_C = 50$.

APPENDIX B

NIR PHOTON PUMPING

B1. EFFECT ON ROTATIONAL LEVELS OF CO AND H_2O

The near-infrared pumping of the CO molecule (and in general a simple diatomic molecule) is derived using a five-level system: three levels in the vibrational ground state $v = 0$ with rotational levels $J - 2$, J, and $J + 2$, the other two in $v = 1$ with rotational levels $J + 1$ and $J - 1$. A molecule in state $(0, J)$ at radius r can be excited by an NIR photon absorption to either level $(1, J - 1)$ or $(1, J + 1)$ at a rate $B^{0,1}_{J,J+1} I_{J+1,J}$ or $B^{0,1}_{J,J-1} I_{J-1,J}$, where $I_{J+1,J}$ is the NIR mean intensity at r, given by

$$I_{J+1,J} \sim \sum_{\tau_{NIR}=1}^{n} \left\{ \frac{2h\nu^3_{J+1,J}}{c^2} W_d \exp(-\tau_{NIR}) \left[\exp\left(\frac{h\nu_{J+1,J}}{kT_{NIR}} \right) - 1 \right]^{-1} \right\}, \tag{29}$$

where ν is the frequency of the transition from $(1, J + 1)$ to $(0, J)$, W_d is the dilution factor, and τ_{NIR} is the dust optical depth from r to r_{NIR} ($\leq r$), where the dust temperature is T_{NIR}. The frequency ν in first approximation can be written as $\nu_V + \nu^{0,0}_{J+1,J}$, where $h\nu_V$ is the energy of the first vibrational level and $h\nu^{0,0}_{J+1,J}$ is the energy of the pure rotational transition. The dilution factor W_d is given by

$$W_d = \frac{1}{2} \left\{ 1 - \left[1 - \left(\frac{r_{NIR}}{r} \right)^2 \right]^{1/2} \right\}^{-1}. \tag{30}$$

Therefore, the NIR mean intensity at r is the sum of the dust emission from r to a distance at which the dust optical depth is equal to n, weighted for the dilution factor and dust extinction. The sum is carried out over steps of optical depth equal to unity at the NIR wavelength. In practice, we integrate to values of n corresponding to the dust evaporation radius or to $n = 5$, whichever occurs first.

From the vibrationally excited state, the molecule can decay to $(0, J + 2)$, $(0, J)$ or $(0, J - 2)$ at a rate given by the spontaneous emission coefficient $A^{1,0}_{J+1,J}$ or $A^{1,0}_{J+1,J+2}$ or $A^{1,0}_{J-1,J}$ or $A^{1,0}_{J-1,J-2}$. Calling $R_{J,J+2}$ the net rate per molecule being pumped from $(0, J)$ to $(0, J + 2)$ and $f^{1,0}_{J+1,J+2}$ the fraction that decay from $(1, J + 1)$ to $(0, J + 2)$, it follows that

$$R_{J,J+2} = B^{0,1}_{J,J+1} I_{J+1,J} f^{1,0}_{J+1,J+2}, \tag{31}$$

where

$$f^{1,0}_{J+1,J+2} = \frac{A^{1,0}_{J+1,J+2} + B_{J+1,J+2} I_{J+2,J+1}}{A^{1,0}_{J+1,J+2} + B^{0,1}_{J+1,J+2} I_{J+2,J+1} + A^{1,0}_{J+1,J} + B^{0,1}_{J+1,J} I_{J+1,J}}. \tag{32}$$

Substituting equations (32) and (29) into (31), we find

$$R_{J,J+2} = \frac{g_{J+1}}{g_J} A^{1,0}_{J+1,J} t_{J+1,J} \left(1 + \frac{A^{1,0}_{J+1,J}}{A^{1,0}_{J+1,J+2}} \frac{1 + t_{J+1,J}}{1 + t_{J+2,J+1}} \right)^{-1}, \tag{33}$$

where

$$t_{J+1,J} = W_d \exp(-\tau_{NIR}) \left[\exp\left(\frac{h\nu_{J+1,J}}{kT_{NIR}} \right) - 1 \right]^{-1}. \tag{34}$$

Analogously, it holds that

$$R_{J,J-2} = \frac{g_{J-1}}{g_J} A^{1,0}_{J-1,J} t_{J-1,J} \left(1 + \frac{A^{1,0}_{J-1,J}}{A^{1,0}_{J-1,J-2}} \frac{1 + t_{J-1,J}}{1 + t_{J-2,J-2}} \right)^{-1}. \tag{35}$$

Equations (33) and (35) can be generalized for H_2O to

$$R_{u,l} = \sum_n \frac{g_n}{g_u} A^{1,0}_{n,u} t_{n,u} f_{n,l}, \tag{36}$$

where

$$f_{n,l} = \frac{A^{1,0}_{n,l}(1 + t_{n,l})}{\Sigma_m A^{1,0}_{n,m}(1 + t_{n,m})}. \tag{37}$$

B2. CO HEATING

A simplified approximated expression can be derived in the case of the CO molecule assuming LTE in the rotational levels. In fact, in this case each NIR photon-induced transition from J to $J+2$ or $J+2$ to J is converted quickly to heating (cooling) by the collisions that de-excite (excite) the population back to LTE. Each transition $J+2$, J contributes to the net heating with a term

$$\Gamma_J = E_{J+2,J}(n_J R_{J,J+2} - n_{J+2} R_{J+2,J}) , \tag{38}$$

where $E_{J+2,J}$ is the energy difference between $J+2$ and J. Making the approximation that the energy of the $v=1$ level ($E_v \simeq 3000$ K) is greater than the energy of the J pure rotational level (strictly valid for $J \leq 20$) and that the spontaneous emission coefficient from any $v=1$ J rotational level to the corresponding $v=0$ $J=J-1$ or $J+1$ rotational level is constant and equal to A_v, the $R_{J,J+2}$ and $R_{J+2,J}$ rates can be simplified to

$$R_{J,J+2} \simeq \frac{A_v}{2} \frac{g_{J+1}}{g_J} t_{J+1,J} , \tag{39}$$

$$R_{J+2,J} \simeq \frac{A_v}{2} \frac{g_{J+1}}{g_{J+2}} t_{J+1,J+2} . \tag{40}$$

Making the further approximation $E_v \gg kT_{\rm NIR}$, equation (38) can be rewritten as

$$\Gamma_J = n_J A_v W_d e^{-\tau_{\rm NIR}} e^{-E_v/kT_{\rm NIR}} E_0 \frac{(2J+3)^2}{2J+1} [e^{-2E_0(J+1)/kT_{\rm NIR}} - e^{2E_0(J+2)/kT_{\rm NIR} - 2E_0(2J+3)/kT_{\rm CO}}] , \tag{41}$$

where the excitation energy level of the J level is $E_J = E_0 J(J+1)$. The total cooling from CO becomes

$$\Gamma_{\rm CO} = n_{\rm CO} A_v W_d e^{-\tau_{\rm NIR}} e^{-E_v/kT_{\rm NIR}} E_0 \sum_J \frac{(2J+3)^2}{Z} e^{-E_0(J+1)J/kT_{\rm CO}} [e^{-2E_0(J+1)/kT_{\rm NIR}} - e^{2E_0(J+2)/kT_{\rm NIR} - 2E_0(2J+3)/kT_{\rm CO}}] , \tag{42}$$

where Z is the partition function. The sum vanishes when $T_{\rm NIR} = T_{\rm CO}$, i.e., when the gas and dust temperature are equal, as expected, and for small differences in the temperatures the heating can be approximated by

$$\Gamma_{\rm CO} \simeq n_{\rm CO} A_v W_d e^{-\tau_{\rm NIR}} e^{-E_v/kT_{\rm NIR}} 2 \left(\frac{E_0}{kT_{\rm NIR}}\right)^3 (kT_{\rm NIR} - kT_{\rm CO}) \sum_J (2J+3)^3 e^{-E_0(J+1)(J+2)/kT_{\rm NIR}} . \tag{43}$$

In the other limit of $T_{\rm NIR} \gg T_{\rm CO}$, the sum in equation (42) tends to 8, and the heating becomes

$$\Gamma_{\rm CO} \simeq 8 n_{\rm CO} A_v W_d e^{-\tau_{\rm NIR}} e^{-E_v/kT_{\rm NIR}} E_0 . \tag{44}$$

Note that in the case of a continuous range of $\tau_{\rm NIR}$ and $T_{\rm NIR}$ for the source of the NIR pumping, such as in our case of infall, a sum such as given in equation (29) is required to approximate the total heating.

REFERENCES

Abouelaziz, H., Gomet, J. C., Pasquerault, D., Rowe, B. R., & Mitchell, J. B. A. 1993, J. Chem. Phys., 99, 237
Adams, F. C., & Shu, F. H. 1985, ApJ, 296, 655
———. 1986, ApJ, 308, 836
Allamandola, L. J., Tielens, A. G. G. M., & Barker, J. B. 1989, ApJS, 71, 733
André, P., Ward-Thompson, D., & Barsony, M. 1993, ApJ, 406, 122
André, P., & Montmerle, T. 1994, ApJ, 420, 837
Barsony, M., & Chandler, C. J. 1993, ApJ, 406, L71
Bell, K. R., & Lin, D. N. C. 1994, ApJ, 427, 987
Bertout, C., & Basri, G. 1989, in The Physics of Star Formation and Early Evolution, ed. C. J. Lada & N. D. Kylafis (Dordrecht: Kluwer), 649
Brown, P. D., Duley, W. W., Jones, A. P., & Williams, D. A. 1989, MNRAS, 241, 753
Burke, J., & Hollenbach, D. J. 1983, ApJ, 265, 223
Butner, H. M., Evans, N. J. I., Lester, D. F., Levrault, R. M., & Strom, S. E. 1991, ApJ, 376, 636
Castor, J. I. 1970, MNRAS, 149, 111
Ceccarelli, C., Haas, M., Hollenbach, D. J., & Rudolph, A. 1996, ApJ, submitted
Chackerian, G., & Tipping, J. 1983, J. Mol. Spectrosc., 99, 431
Charnley, S. B., Tielens, A. G. G. M., & Millar, T. J. 1992, ApJ, 399, 71
Choi, M., Evans N. J. II., Gregersen, E. M., & Wang, Y. 1995, ApJ, 448, 742
Cohen, M., Hollenbach, D. J., Haas, M. R., & Erickson, E. F. 1988, ApJ, 329, 863
Draine, B. T. 1988, in Infrared Spectroscopy in Astronomy, Proc. 22d ESLAB Symposium, ed. M. Kessler (ESA SP-290), 93
Draine, B. T., & Sutin, B. 1987, ApJ, 320, 803
Flower, D. R., & Launay, J. M. 1985, MNRAS, 214, 271
Galli, D., & Shu, F. H. 1993a, ApJ, 417, 220
———. 1993b, ApJ, 417, 243
Gear, C. W. 1971, Numerical Initial Value Problems in Ordinary Differential Equations (Englewood Cliffs: Prentice-Hall)
Gerola, H., & Glassgold, A. E. 1978, ApJS, 37, 1
Grachev, S. I., & Grinin, V. P. 1975, Astrophysics, 11, 20
Green, S., Maluendes, S., & McLean, A. D. 1993, ApJS, 85, 181
Hartmann, L. W., & Kenyon, S. J. 1990, ApJ, 349, 190
Hollenbach, D. J., & McKee, C. F. 1979, ApJS, 41, 555
Hollenbach, D. J., Takahashi, T., & Tielens, A. G. G. M. 1991, ApJ, 377, 192
Jenkins, E. B., Jura, M., & Loewenstein, M. 1983, ApJ, 270, 88
Kaufman, M. J., & Neufeld, D. A. 1996, ApJ, 456, 611
Koorneef, J. 1983, A&A, 128, 84
Launay, J. M., & Roeuff, E. 1977, A&A, 56, 289
Lepp, S., & Dalgarno, A. 1988, ApJ, 324, 552
Lin, D. N. C., & Pringle, J. E. 1990, ApJ, 358, 515
Lizano, S., & Shu, F. H. 1989, ApJ, 342, 834
Marti, F., & Noerdlinger, P. D. 1977, ApJ, 217, 247
McKee, C. F., Storey, J. W. V., Watson, D. M., & Green, S. 1982, ApJ, 259, 647
Millar, T. J., Rawlings, J. M. C., Bennet, A., Brown, P. D., & Charnley, S. B. 1991, A&AS, 87, 585
Natta, A. 1993, ApJ, 412, 767
Omont, A. 1986, A&A, 164, 159
Peimbert, M. 1982, in The Orion Nebula (Ann. NY Acad. Sci., Vol. 359), 24
Rothman, L. S., et al. 1987, Appl. Opt., 26, 4058
Rybicki, G. B., & Hummer, D. G. 1978, ApJ, 219, 654
Saraceno, P., André, P., Ceccarelli, C., Griffin, M., & Molinari, S. 1996, A&A, in press
Schuster, K. F., Harris, A. I., Anderson, N., & Russel, P. G. 1993, ApJ, 412, L67
Shu, F. H. 1977, ApJ, 214, 488
Shu, F. H., Najita, J., Ruden, S., & Lizano, S. 1994b, ApJ, 429, 797
Shu, F. H., Najita, J., Ostriker, E. C., Wilkin, F., Ruden, S., & Lizano, S. 1994a, ApJ, 429, 781
Stahler, S. W. 1988, ApJ, 332, 804
Stahler, S. W., Shu, F. H., & Taam, R. E. 1980, ApJ, 241, 637

Takahashi, T., Hollenbach, D. J., & Silk, J. 1983, ApJ, 275, 145
Tarafdar, S. P., Huntress, W. T., Villere, K. R., & Black, D. C. 1985, ApJ, 289, 220
Terebey, S., Shu, F. H., & Cassen, P. 1984, ApJ, 286, 529
Terebey, S., Vogel, S. N., & Myers, P. C. 1992, ApJ, 390, 181
Tielens, A. G. G. M. 1993, in Dust and Chemistry in Astronomy, ed. T. J. Miller & D. H. Williams (Bristol: IOP), 189
Tielens, A. G. G. M., & Hollenbach, D. J. 1985, ApJ, 291, 722
Wagner, A. F., & Graff, M. M. 1987, ApJ, 317, 423
Walker, C. K., Narayan, G., & Boss, A. 1994, ApJ, 431, 767
Whitney, B. A., & Hartmann, L. 1993, ApJ, 402, 605
Wilking, B. A., Claussen, M. J., Benson, P. J., Myers, P. C., Tereby, S., & Wootten, A. 1994, ApJ, 431, L119
Wolfire, M. G., & Cassinelli, J. P. 1986, ApJ, 310, 207
Wootten, A. 1989, ApJ, 337, 858
Zhou, S. 1992, ApJ, 394, 204
———. 1995, ApJ, 442, 685
Zhou, S., Evans, N. J., Kompe, C., & Walmsley, C. M. 1993, ApJ, 404, 232